Quantitative and qualitative evaluation of photoreceptor synapses in developing, degenerating and regenerating retinas

(正常発達・変性および再生網膜における視細胞シナプスの定量・定性評価)

千葉大学大学院医学薬学府
先端医学薬学専攻
（主任：山本修一教授）

秋葉龍太朗

Abstract

Quantitative and qualitative evaluation of synapses is crucial to understand neural connectivity. This is particularly relevant now, in view of the recent advances in regenerative biology and medicine. There is an urgent need to evaluate synapses to access the extent and functionality of reconstructed neural network. Most of the currently used synapse evaluation methods provide only all-or-none assessments. However, very often synapses appear in a wide spectrum of transient states such as during synaptogenesis or neural degeneration. Robust evaluation of synapse quantity and quality is therefore highly sought after. In this paper we introduce QUANTOS, a new method that can evaluate the number, likelihood, and maturity of photoreceptor ribbon synapses based on graphical properties of immunohistochemistry images. We used QUANTOS to evaluate synaptogenesis in developing and degenerating retinas, as well as *de novo* synaptogenesis of mouse iPSC/ESC-retinas after transplantation to a retinal degeneration mouse model. Our analysis shows that while mouse iPSC/ESC-retinas are largely incapable of forming synapses *in vitro*, they can form extensive synapses following transplantation. The *de novo* synapses detected after transplantation seem to the in an intermediate state between mature and immature compared to wildtype retina. Furthermore, using QUANTOS we tested whether environmental light can affect photoreceptor synaptogenesis. We found that the onset of synaptogenesis was earlier under cyclic light (LD) condition when compared to constant dark (DD), resulting in more synapses at earlier developmental stages. The effect of light was also supported by micro electroretinography showing larger responses under LD condition.

The number of synapses was also increased after transplantation of mouse iPSC/ESC-retinas transplantation to *rd1* mice under LD condition. Our new probabilistic assessment of synapses may prove to be a valuable tool to gain critical insights into neural-network reconstruction and help develop treatments for neurodegenerative disorders.

Introduction

Recent advances in stem cell biology have overturned the long-held belief that neurons do not regenerate. It has now been established beyond doubt that neural networks can be reconstructed after injury or degeneration either by endogenous regeneration(Jorstad et al. 2017; Yao et al. 2018) or by cell or tissue transplantation(Singh et al. 2013; Barnea-Cramer et al. 2016; Mandai et al. 2017). A critical step for neural reconstruction is the requirement for these newly formed or reintroduced neurons to form new chemical synapses. Current methods are however, insufficient to evaluate the extent of neural integration, and more sophisticated methods to evaluate neural integration are in demand.

A chemical synapse is a subcellular structure specialized for communication between neurons through neurotransmitter molecules. As a key parameter to evaluate the functional state of neural networks, various methods have been developed to quantify and assess synapses over the years. The gold standard to assess the state of a synapse is by electron microscopy (EM), where subcellular pre- and post-synaptic components can be directly observed (Geinisman et al. 1996). While EM can provide valuable qualitative information about the state of a particular synapse, it is currently unpractical to survey a large number of synapses, especially if their rough locations are not known. On the other hand, visualization of pre- and post-synaptic markers by immunohistochemistry (IHC) allows for a robust and high throughput analysis, while simultaneously obtaining some qualitative information.

One of the most common approaches to quantifying synapses by IHC is to manually count pre- and post-synaptic marker pairs (Silver and Stryker 2000; Ribic et al. 2014). Although

laborious, a trained expert may be able to reliably count synapses, but different observers may naturally focus on different features and have different thresholds of acceptance. The use of automated software for quantification is another alternative, for example by counting the number of co-localized pre- and post-synaptic markers (Dominic M Ippolito 2010). These automatic counting programs apparently seem free of human bias, but certain choices are inevitably made by the software or software developers with or without the user's knowledge. For example, colocalization-based classifiers require binary images where pixels are assigned as stained or unstained for a marker. Binary images are constructed by thresholding the original images by manually adjusting a threshold level (Glynn and McAllister 2006) or by selecting one of many thresholding algorithms, which calculates a threshold level. In either case, only slight differences in the threshold level can result in drastically different output counts. Different conditions in recording and staining also cause diverse estimates when the same threshold level is applied (Glynn and McAllister 2006). A third and more modern approach is machine learning-guided automatic classification methods, which enabled more reproducible analysis (Fantuzzo et al. 2017). However, it is usually unclear what the machine is "learning", and the factors involved in the decision making of the algorithm are typically unknown. Above all and most unfortunately, all these synapse quantification methods typically assign a binary value to the marker pairs, either as synapses or not, without accounting for any immature or intermediate properties which however do exist, as exemplified in retinal synaptogenesis, where photoreceptors and bipolar cells form synapses through retinal development(Regus-Leidig et al. 2009). A trained expert can discern these immature or

transient states from the morphological, geometrical, and signal intensity properties of an IHC image, allowing for a more nuanced interpretation than the mere number of synapses. Furthermore, there is an increasing need in assessing synapse formation in the field of neural regeneration and cell therapies that involves reconstruction of neural networks by neural cells from endogenous regeneration or transplantation, where the quantitative and qualitative synapse evaluation is considered most relevant to *de novo* neural function. We previously showed that transplantation of mouse ES or iPS derived retinas (mESC/miPSC-retinas) could restore light response in the end-stage retinal degeneration mouse models with some evidence of host-graft synaptic connection (Assawachananont et al. 2014; Mandai et al. 2017; Iraha et al. 2018). A quantitative and qualitative evaluation of synapses would therefore provide a strong clue for estimating the functional potency of grafted tissues, and would further help optimize and develop better conditions for this therapeutic approach.

We thus propose a probabilistic evaluation of synapses from IHC images, which would allow us not only to quantify the number of synapses but also to estimate the likelihood of "synapse-ness" based on multi-synaptic factors on a continuous scale. We named this approach QUANTOS (QUalitative and quantitative ANalysis using Bayes Theorem Optimized for Synapse evaluation). The QUANTOS analysis specializes in the distinctive synapse structure called "ribbon synapse" located between photoreceptors and bipolar cells, namely the first and the second order neurons in the retina. Ctbp2 is a main component of RIBEYE, with the characteristic horseshoe shape and molecular machinery at the photoreceptor axon terminal that stores and releases glutamate

efficiently to the synaptic cleft(tom Dieck et al. 2005; Matthews and Fuchs 2010). Metabotropic glutamate receptor type 6 (mGluR6) is expressed on dendritic tips of ON-bipolar cells to receive the glutamate released from the photoreceptors (Sterling and Matthews 2005). We used IHC images of presynaptic RIBEYE and postsynaptic mGluR6 to train QUANTOS and thereby analyzed photoreceptor-bipolar ribbon synapses.

In order to showcase QUANTOS, we first studied the impact of light, i.e., photoreceptor activity on the ribbon synapse formation during development, to test the famous adage: "neurons wire together if they fire together" (Lowel and Singer 1992). Electrophysiology was tested in parallel to see the physiological relevance of our synapse assessment. We then used QUANTOS to quantify and assess synaptogenesis of mESC/iPSC-retinas after transplantation in the *rd1* mice with end stage retinal degeneration. Here again we tested whether light influences regenerative synapse formation.

Results

General design of the QUANTOS

The general design of the method is described in Fig. 1 and Figs S1-S5. Samples obtained at different developmental stages were co-stained for pre- and post-synaptic markers, RIBEYE and mGluR6. Images were then processed to isolate regions of interest (ROIs) and graphical information was extracted from each ROI. The training data of synapse and noise was generated from images containing mature synapses, by manually selecting the outer plexiform layer (OPL) from the rest of the retina. This training data was used to create probability density functions (PDF) from the extracted

graphical information, and using these we generated a Naïve Bayes classifier to evaluate the synapse and noise likelihood of each ROI. This allows us to identify the ROIs that are more likely to be synapses based on the training data and estimate the total amount of synapses as well as their individual synapse likelihood. The example IHC image of P28 C57BL/6J (B6J) mouse indicates where the synapses were detected by QUANTOS (Fig. 2e).

Graphical properties of the ribbon synapse

PDFs generated from the training data revealed the properties of noise and synapse staining. The distribution of synapse distances between pre- and post-synaptic makers indicate that synapse distances have a Gaussian distribution with a mean distance of 0.51 μm and a standard deviation of 0.17 μm (Fig. 2a). From our simulation of random markers, the noise distribution was approximated with a polynomial function of second order; however, noise distances were not necessarily distributed randomly, as noise signals tended to be clustered. The noise angle distribution had a uniform distribution as expected from a random distribution, whereas the synapse angle distribution indicated that the major population of synapses were aligned vertically. Interestingly, the synapse angle distribution had a wide tail indicating synapses at various angles, even horizontally aligned or vertically aligned but in opposite directions (Fig. 2b). Supplemental Fig. 5 shows the PDFs for *Geometry*, *Morphology*, and *Signal* features. The synapse *area* distributions had distinctive acute peaks, whereas noise *area* distributions had more larger values for both markers. On the other hand, the *integrated*

density was larger in the synapse distribution for both pre- and post-synaptic markers, indicating that noise is either relatively small and bright or large but weakly stained. Many of the *Morphology* parameters, such as *perimeter*, *width*, *height*, *major*, and *minor*, had a broad distribution for noise and a more defined distribution for synapse indicating that noise features are more randomly distributed whereas synapse features do have characteristic staining patterns. Noise distributions for *mean*, *mode*, *median*, *min*, *max*, and *stdev* parameters tended to have a large peak around small values with a long tail extending to large values. Synapse distributions, on the other hand, were more symmetric and centered around larger values.

Evaluation of QUANTOS

We evaluated the sensitivity and specificity of QUANTOS, using a manually curated data set of synapses on postnatal day (P) 14 and P28, which represent emerging and mature synapses respectively. Several receiver operating characteristics (ROC) curves using combinations of *Signal*, *Morphology*, and *Geometry* parameter categories were generated to better understand the features contributing information to the classifier. Ground truths for P14 and P28 samples were generated by careful evaluation by an expert observer. The ROC curve for the distance parameter alone performed very poorly with an area under that curve (AUC) of 0.55 (95% confidence interval (CI): 0.51-0.58), indicating that the distance-based classifier performance is close to random chance. Adding *Morphology* and *Geometry* parameters increased the AUC to 0.89 (CI: 0.87-0.92) and 0.95 (CI: 0.93-0.97), respectively. While both parameter categories increased

classifier performance substantially, inclusion of *Morphology* seemed to favor sensitivity, whereas *Geometry* enhanced specificity. Among the three categories of parameters, *Signal* parameters showed the largest AUC value of 0.98 (CI: 0.98-0.99), suggesting that *Signal* parameters contained the most information. The best AUC (0.99, CI: 0.98-0.99) was obtained when all the parameters were used (Fig. 2c). A similar trend was observed in the P14 sample (Fig. 2d), where the largest AUC value was 0.97 (CI:0.96-0.98) for the classifier utilizing all the parameters, indicating that QUANTOS was able to reliably evaluate immature synapses in developing retinas.

We also compared QUANTOS against manual counting. Three observers manually counted synapses, and their results were matched with the ground truth for estimating the specificity and sensitivity. QUANTOS outperformed manual counts with a small margin, consistently in both P28 (Fig. 2c) and P14 (Fig. 2d) images. Manual counting varied in the specificity and sensitivity properties, and the difference was more pronounced on P14, suggesting that human assessment is less stable when encountering immature developmental synapse data. On the other hand, QUANTOS showed robust performance both for immature and mature developmental stages.

Quantification of the photoreceptor ribbon synapse during postnatal development of B6J mice under different light conditions

We first used QUANTOS to quantify synapse formation in wildtype B6J mice reared under cyclic light (LD) and constant dark (DD). IHC images of B6J mice on different postnatal days showed that immunoreactivities of RIBEYE and mGluR6 were weak and

diffuse on P7, but became stronger on P10. The characteristic horseshoe shape of RIBEYE could be observed after P14, and mGluR6 expression pattern also became punctate on P14. By P21, the shape of the synapse was defined, and the same expression pattern was maintained through P28 and P35 (Fig. 3a). QUANTOS detected almost no or very few synapses on P7 and P10 either under LD or DD conditions. From P14 to P21, the number of synapses rapidly increased and remained largely constant through P28 and P35 (Fig. 3b). Notably, samples acquired from mice reared in LD condition tended to have more synapses on P10 and P14. We thus modeled the process of synaptogenesis with a growth curve to analyze the effect of light (Fig. 3e) using Bayesian parameter estimation. The model shows that while the maximum rate of synaptogenesis (μ_M) and the maximum number of synapses (A) were not significantly different between LD and DD conditions, the onset of synaptogenesis (λ), on the other hand, was faster in LD condition by about one day (Figs. 3c and 3d), indicating that light influences synaptogenesis.

Quality changes of the photoreceptor ribbon synapse during postnatal development of B6J mice under different light conditions

We then inspected the distributions of the likelihoods of synapses determined by QUANTOS in all synapse candidates (Fig. 3f). The horizontal axis shows the log synapse likelihood and the vertical axis represents log noise likelihood. The diagonal line represents the boundary where the probability of synapse and noise are equal. On P7, synapse candidates clearly had a peak towards the noise, but from P14 onwards, a

second peak with high synapse probability appeared. The synapse peak kept increasing after P21, becoming more prominent on P28 (Fig. 3f). Similar trends were observed under both LD and DD conditions.

Lastly, we visualized different states of developmental ribbon synapses by creating average images from all the detected synapses (Fig. 3g). RIBEYE and mGluR6 showed diffuse expression patterns on P7 and P10, which became more focused on P14 and later postnatal stages under both LD and DD conditions. The intensity plot against distance from center coordinates of pre- and post-synaptic markers showed that signal intensity became higher at later postnatal stages under both conditions (Fig. 3h).

Effect of light assessed by micro electroretinography (mERG)

In order to determine if the difference in synapse numbers suggested by QUANTOS was physiologically relevant, we recorded the mERG response of P14 retinas, as the difference in synapse numbers was most prominent between LD and DD at this stage. The b-wave, an upward peak between 150 ms after the onset of light pulse stimulation is derived from the ON-bipolar cells that receive signal inputs from photoreceptors through ribbon synapses (Fig. 4a). We compared the amplitude of b-waves across mice reared in DD, LD, or constant light (LL) conditions. The histograms of b-wave amplitudes showed a skewed distribution towards smaller values (Fig. 4b, upper), with LD and LL having longer tails towards larger b-wave amplitudes. We modeled the data with a hierarchical generalized linear Gamma model (Fig. 4b, lower), showing a reasonable summary of b-wave amplitudes. Our model indicates that both the mean

value of the b-wave amplitude (Fig. 4c), and its standard deviation (Fig. 4e) were significantly higher in LD and LL when compared to DD condition (Figs. 4d and 4f). This is consistent with the quantitative evaluation of photoreceptor ribbon synapses in P14 retinas by QUANTOS, suggesting that the presence of light may accelerate development of photoreceptor ribbon synapses.

Evaluation of photoreceptor ribbon synapses in the progressive retinal degeneration model (rd1) during development and degeneration

One potential application of QUANTOS is to evaluate the synapse formation after transplantation of ES/iPS derived retinas in retinal degeneration models. We first quantified photoreceptor ribbon synapses in *rd1* mouse retinas, in which rod photoreceptors are mostly lost in the first 4 postnatal weeks. IHC images of *rd1* retinas on P7 showed weak expression of RIBEYE, which became prominent on P10, showing some horseshoe shape patterns (Fig. 5a). However, the RIBEYE expression decreased from P14, leaving almost no signals by P28. On the other hand, the expression of mGluR6 was constantly weak throughout all postnatal stages. The number of synapses quantified by QUANTOS are shown in Fig. 5b together with the B6J data (LD condition) for comparison. Results of *rd1* retinas quantification showed a slight increase of synapses from P7 to P14, followed by a gradual decrease thereafter. The number of synapses in *rd1* was dramatically reduced by P28 compared to B6J. The number of ONL cells started decreasing on P14 and continued to decrease through P21 and P28

(Fig. 5c). ONL cells did not completely disappear even on P28, probably because cone photoreceptors survive longer than rods.

Next, we generated 2D histograms of synapse and noise log likelihoods for all the synapse candidates. While synapses seemed to increase toward P14 in *rd1*, no distinctive synapse group was observed as in the wildtype, suggesting that synapses formed in *rd1* are incomplete and small in number compared to B6J (Fig. 5d). We again visualized synapses from different postnatal days by averaging all the synapses detected by QUANTOS (Fig. 5e). The signal of RIBEYE transiently increased in size on P14, but then continuously decreased through P21 and P28. mGluR6 expression did not noticeably change from P7 to P21, but slightly decreased on P28. Signal intensity of averaged synapses were plotted against the distance from the center of synaptic makers (Fig. 5f). These plots show that the intensity peak became higher on later postnatal days in B6J, but the opposite trend was found in *rd1* mice, showing lower intensity on later postnatal days for both synaptic markers.

Quantity and quality change of ribbon synapses after subretinal transplantation of miPSC-retinas into rd1 and the effect of light on regenerative synaptogenesis

We transplanted miPSC-retinas of differentiation day (dd) 12-13 into 9 to 12-week-old *rd1* mice, and then investigated synaptogenesis by IHC on post-transplantation days (PT) 14, 30, and 60 (approximately equivalent to dd26, 42, and 72). IHC images from PT14 retinas showed immature expression of RIBEYE and almost no expression of mGluR6 (Fig. 6a). On PT30 and PT60, typical horseshoe shaped RIBEYE and punctate

mGluR6 immunoreactivities were observed surrounding the transplants, suggesting the formation of synapses (Figs. 6b and 6c). We first examined dd25 and dd36 samples by QUANTOS to test if miPSC-retinas could form synapses *in vitro*, and found that there was almost no synapse formation *in vitro* regardless of differentiation day (Fig. 6d, left). In contrast, a substantial number of synapses was formed in the post-transplantation *rd1* retinas (Fig. 6d, middle). The number of synapses per graft photoreceptor increased substantially from PT14 to PT30 and then to PT60, indicating that transplanted photoreceptors form new synapses as miPSC-retinas integrate and mature in the host *rd1* retinas. We also tested the effect of light on post-transplantation synaptogenesis and found that the number of synapses per photoreceptor was higher in LD condition on PT60, indicating that that similarly to developmental B6J retina, light resulted in an increased number of synapses (Figs. 6d-f). In one sample of *rd1* mouse (60 days after miPSC-retina transplantation, reared on DD), grafted cells lined up horizontally and formed an ONL-like structure with a plexiform layer resembling the OPL in wildtype retinas (Fig. 7a). To identify whether these *de novo* synapses include host-graft synapses, we used L7-GFP/*rd1-2J* mice as host animals and Nrl-GFP/ROSA::Nrl-CtBP2-tdTomato mESC-retinas as transplants. The IHC image indeed showed that host rod bipolar cells extended their dendrites and formed ribbon synapses with graft photoreceptor cells (Fig. 7b).

2D histograms of noise and synapse likelihoods of *in vitro* miPSC-retinas showed sparse synapse candidates distributed in the noise region, and almost no candidates toward synapse were observed on dd25 and dd36 samples (Fig. 6g). After

transplantation, synapse candidates were observed mostly toward synapse on P14, with LD-conditioned mice having more candidates toward synapse. On P30, a small peak was observed towards higher synapse likelihood in both LD and DD. The small synapse peak remained in the LD samples on PT60, but was less prominent in the DD condition.

For visualization of the expression pattern, all synapses detected by QUANTOS were averaged (Fig. 6h). Before transplantation, the expression pattern of RIBEYE from *in vitro m*iPSC-retinas was diffuse on dd25, but became more focused on dd36. mGluR6 expression was quite weak both on dd25 and on dd36. After transplantation, the expression pattern of RIBEYE became larger and brighter, but mGluR6 expression was relatively weak on all post-transplantation days. This trend was confirmed by intensity plots (Fig. 6i). The intensity of RIBEYE became higher on later post-transplantation days, but the intensity of mGluR6 was low throughout all time points, when compared to the B6J LD condition.

Mature/immature likelihoods of synapses

We built a synapse classifier using synapse and noise training data. Similarly, we attempted to further discriminate synapses by training a new classifier with P10 (DD) and P28 (LD) synapses, representing relatively immature and mature synapses respectively. Samples of B6J during development under DD/LD conditions and *rd1* after transplantation of miPSC-retina were tested for this analysis. 2D histograms of mature and immature synapse likelihoods of the B6J mice show an immature small population dominantly on P10 which starts to shift toward the mature region in the LD

condition on P14, but it is delayed in the DD condition (Fig. 8a). This suggests that LD synapses acquire mature properties earlier than DD synapses. The majority of the synapses were classified on the mature side by P21 in both LD and DD conditions. Synapses in postnatal *rd1* mice exhibited a mixture of mature and immature properties (Fig. 8b). Synapses in *rd1* mice after miPSC-transplantation were more diverse in mature/immature likelihoods, but some showed higher mature likelihood (Fig. 8c). When the log likelihoods of mature and immature synapse were plotted separately for pre- and post-synaptic markers, the pre-synaptic marker population is shifted toward mature from PT14 to PT30, suggesting expression of more mature RIBEYE in iPSC-retina after transplantation (Fig. 8d).

Discussion

In the present study, we introduced our new synapse evaluation method using a Naïve Bayes classifier, "QUANTOS", which offers a transparent evaluation of multiple parameters, thereby achieving a reproducible and robust counting of retinal ribbon synapses. Many synapse classifiers are simply colocalization-based, however spatial information alone is not enough to reliably evaluate synapses. Our data indicate that the mean distance between pre- and post-synaptic markers in the photoreceptor ribbon synapse is 0.51 μm, which is consistent with a previously reported distance of 400 nm to 800 nm for mGluR6 and presynaptic active zone in an EM study (Vardi et al. 2000). The identification of overlapping markers depends largely on the adjustment of the threshold which is arbitrary and unstable as evidenced by the ROC curve of the distance-based

classifier, which showed near random chance performance. In manual counting, the counter is evaluating multiple parameters simultaneously and setting thresholds of acceptance for those features based on the present image and prior experience. These assessment criteria are often difficult to articulate, and different observers may place importance on different features. Our present approach is more transparent as all the parameter PDFs are defined, and the user may trace back the features that contribute to a particular synapse assessment. QUANTOS allows users to see which parameters and how those parameters are changing during synaptogenesis, and what is causing the difference between synapse and noise, or mature and immature synapses.

We originally intended to only use parameters that had large differences in their synapse and noise PDFs. However, ROC analysis revealed that the largest AUC is obtained when all the parameters are employed. In fact, while the *Signal* parameters alone have an excellent AUC, the *Morphology* and *Geometry* parameters combined also have a considerable AUC, indicating that features other than the signal parameters also contain valuable information. Even when the difference between synapse and noise PDFs is small for individual parameters, they may contain significant information when combined. Another advantage of using a large number of parameters is that QUANTOS is more robust as it is less reliant on a particular trait. This robustness is well illustrated by the selection process of the synapse, where many parameters detect different synapse candidates, but only the ones in the OPL were selected in the end (Fig. 2f). In practical comparison, it is interesting that manual counts fall very near along the ROC curve, indicating that QUANTOS is making a very similar trade-off between sensitivity and

selectivity to a human observer; however, as its parameters are well defined, it is highly reproducible, unlike manual counts.

The noise/synapse classification revealed two separate populations (Fig. 3f); the mature/immature classifier, on the other hand, did not reveal such discrete groups (Fig. 8). This indicates that immature and mature synapses exist on a continuum with no clear boundaries, at least regarding their IHC properties. While our definition of mature and immature synapses is completely arbitrary, we were still able to observe a shift from more immature to more mature synapses along retinal development, which would have been impossible to observe with traditional synapse classifiers. Furthermore, the characterization of mature/immature synapse properties by QUANTOS was also consistent with the reported developmental features of the photoreceptor ribbon synapse. An EM study reported that development of the photoreceptor ribbon synapse starts around P4, but the photoreceptors only form dyads with horizontal cells at this stage. Later, around P7 to P14, dendrites of bipolar cells invaginate into the dyad and make triads, which makes the photoreceptor ribbon synapse complete. The number of triads starts increasing from P7 to P14, and shows a gradual decrease afterwards(Blanks, Adinolfi, and Lolley 1974). Another IHC study showed that the number of mGluR6 puncta rapidly increases in the first two postnatal weeks, and plateaus around P21 (Anastassov, Wang, and Dunn 2017). Consistent with these reports, we found that the majority of the synapses were classified as mature by P21.

Furthermore, we used QUANTOS to quantify the photoreceptor ribbon synapses formed under different light conditions in relevance to the physiological function of

photoreceptors. There are conflicting reports on the effect of light on photoreceptor synapses. In adult mice, photoreceptor ribbon synapses increase with continuous illumination when observed by EM, but this is thought to be illumination-dependent detachment of ribbons from the active zone, and not an increase of synapse numbers (Spiwoks-Becker et al. 2004). Another study using ERG reported that on P30 and P60 a- and b-wave amplitudes decrease in DD reared mice when compared with LD reared mice (Tian 2004). Another mERG study reported that dark rearing does not affect rod-driven b-wave amplitude (Dunn et al. 2013). Our analysis of the effect of light throughout the synaptogenesis period suggests that light is accelerating synapse formation itself. Our mERG recordings support the QUANTOS synapse analysis. These findings suggest that the number and/or function of photoreceptor synapses is enhanced by light. This could be in part due to the delayed maturation of the retinal cells, since it was previously reported that morphological maturation of bipolar cells is delayed by dark rearing (Wu and Chiao 2007). This highlights the sensitivity of QUANTOS, as raw images do not appear noticeably different at first glance. Despite the fact that there is quite a lot of variance between mice, we were able to identify the differences using QUANTOS.

Lastly, we assessed synapse degeneration in the retinal degeneration model *rd1* and regenerative synaptic formation/maturation of transplanted miPSC-retinal tissues. Previous EM studies indicate that early development of *rd1* is normal up to about P10, but later bipolar cell dendrites fail to invaginate photoreceptors (Blanks, Adinolfi, and Lolley 1974). The number of synapses on P28 was dramatically reduced when compared with B6J mice, and the remaining synapses had low likelihood of synapse and low likelihood

of being mature as determined by QUANTOS, suggesting incomplete synapse formation, consistent with past EM studies.

Although miPSC-retina formed no substantial synapses *in vitro*, the number of synapses seemed to increase in a time dependent manner after transplantation, suggesting that these synapses are not the remaining *rd1* host synapses, but newly-introduced synapses formed in transplanted cells. This result indicates that synaptogenesis requires intra-ocular factors that are not present in the *in vitro* environment. This was consistent with a recent study reporting that *in vitro* miPSC-retinas can mature up to an equivalent stage of P6 wildtype retina, but do not show apparent synaptogenesis (DiStefano et al. 2018). Here again, the number of synapses formed after transplantation was enhanced by light, suggesting a positive effect of some visual stimuli after transplantation to boost synapse formation. Detected *de novo* synapses were classified as a mixed population of mature and immature synapses, and these include some host-graft synapses as implied by the use of L7-GFP/*rd1* host mice.

Conclusion

We have established an innovative method, that we have named QUANTOS, to robustly and transparently evaluate the quality and quantity of the photoreceptor ribbon synapse from IHC images. Using this method, we have successfully evaluated developmental synaptogenesis of the wildtype B6J mouse retina, the degenerative process of the *rd1* mouse retina, and regenerative synaptogenesis of the mES/iPSC-retina after transplantation. We showed that miPSC-retina cannot form substantial *de*

novo synapses *in vitro* but it is capable of extensive synaptogenesis after transplantation. We also showed that light has a positive effect both on the quantity and quality of synapses formed during developmental and regenerative synaptogenesis of photoreceptors. Although QUANTOS was optimized for the photoreceptor ribbon synapse in this study, this method can be easily adapted to observe synaptogenesis of other neurons.

Methods

Animals

All animal experiments were conducted in accordance with local guidelines and the ARVO statement on the use of animals in ophthalmic and vision research. All the experimental protocols were approved by the animal care committee of the RIKEN Center for Biosystems Dynamics Research (BDR).

C57BL/6J (B6J) mice were used for developmental analysis, and C57BL/6J-Pde6b$^{rd1\text{-}2J}$/J (*rd1*) mice were used for the retinal degeneration model. We also prepared an end-stage retinal-degeneration model mouse that expresses GFP in rod bipolar cells (*L7*-GFP/rd1) by crossing rd1-2J and *L7*-GFP mice as previously described(Mandai et al. 2017). Enucleation was carried out immediately after sacrificing the animals.

Animals were reared under different illumination conditions to investigate the effect of light on synaptogenesis. In the LD condition, animals were kept under the standard 12 hours light (from 8am to 8pm) and 12 hours dark cyclic light environment. The light

source was a fluorescent light bulb with an irradiance, measured vertically upward from the bottom of the rearing cage, of 67.4μW/cm^2 (233lux). For the DD condition, B6J mice were kept in constant darkness from before birth. For the retinal transplantation experiments, *rd1* mice were maintained in LD condition and then moved to DD condition immediately after transplantation. For the DD condition, all the animal care was carried out using LED lights with peak wavelength of 690 nm, which had a minimal effect on mouse photoreceptors.

Additionally, animals were reared in constant light (LL) condition for micro electroretinography (mERG) analysis. The irradiance was the same as the LD condition, but the light was always kept on in this condition.

Differentiation and subretinal transplantation of mESC/iPSC-retinas

The *Nrl*-GFP miPSC line was generated from transgenic *Nrl*-eGFP mice (Akimoto et al. 2006; Homma et al. 2013) and the *Thy1*-GCaMP6f mESC line was generated from *Thy1*-GCaMP6f transgenic mice(Dana et al. 2014). The Ctbp2:tdTomato fusion protein was expressed under Nrl promoter by introducing the gene on the ROSA 26 locus of these lines as previously described and characterized (Mandai et al. 2017). Maintenance, differentiation and optic vesicle structure preparation for transplantation of Tg(*Nrl*-GFP);ROSA26$^{+/}$*Nrl*-CtBP2:tdTomato and Tg(*Thy1*-GCaMP6f); ROSA26$^{+/}$*Nrl*-CtBP2:tdTomato lines were as previously described (Assawachananont et al. 2014). Briefly, optic vesicle structures (dd 12-13) were cut to small pieces (around 0.5 mm × 2 mm), on the day of transplantation, and inserted sub-retinally into the eye of the 9-12-week-old *rd1* mice

using a glass micropipette with a tip diameter of approximately 500 µm. Indomethacin (10 mg/L) was added to the drinking water of all transplanted mice starting on the day of transplantation.

Immunohistochemistry (IHC)

Animals were sacrificed by cervical dislocation and the eyes were enucleated. The eyes were perforated using a 22G needle, and fixed with 4% paraformaldehyde (PFA) for an hour and then hemisected followed by cryo-protection with 30% sucrose in phosphate buffered saline (PBS) over night at 4°C. The fixed eyes were embedded in OCT compound (4583, Sakura Finetek Japan, Tokyo) and stored at -30 °C. Cryo-sections of 12-µm thickness were made with a Cryostat CM3050S (Leica). Heat induced antigen retrieval was carried out at 100°C for 20 min using citrate buffer (10 mM sodium citrate, pH 6.0). The antigen retrieval process removes fluorescence of all fluorescent proteins. Samples were then blocked with Blocking One (nacalai tesque) with 3% Triton X-100 at room temperature for 1 hour. Samples were next incubated with primary antibodies in 3% Triton X-100/Dako REAL Antibody Diluent (S2022, Dako, Denmark) over 3 nights at 4°C, followed by washing with PBS 5 times. For the primary antibody of the pre-synaptic marker, we used mouse anti-CtBP2 (612044, BD biosciences, Franklin Lakes, NJ, USA). For the primary antibody of the post-synaptic marker, rabbit anti-mGluR6 antibody (AGC-026, Alomone labs, Jerusalem, Israel) was used. Altogether, expressions of RIBEYE and mGluR6 in proximal area were highly indicative of a functional photoreceptor-ON bipolar cell ribbon synapse.

Samples were incubated with secondary antibodies in 3% Triton X-100/Dako REAL Antibody Diluent (S2022, Dako, Denmark) overnight at 4°C, washed with PBS 5 times, and then mounted with FluorSave Reagent (Millipore). Goat anti-mouse IgG Alexa Fluor 546 (Thermo Fisher, Waltham, MA, USA) and goat anti-rabbit IgG Alexa Fluor 647 (Thermo Fisher, Waltham, MA, USA) were used for pre- and post-synaptic marker visualization, respectively. Images were acquired on an inverted confocal microscope Leica-TCS SP8, with oil-immersion 63x objective magnification lens. Resolution of the image was 1024 pixels by 1024 pixels, and 5 sequential z-stacks with 0.3-μm intervals. The z-stack image was acquired by averaging 4 images on each z-plane with frame sequential method. For postnatal samples of B6J and *rd1* mice, the slices containing optic disc were used, and the area 500 μm away from the optic disc was imaged. We fixed the imaging area because retinal development proceeds from the central area to the periphery, and the timing of synaptogenesis might differ depending on the location. For post-transplantation samples of *rd1*, two randomly selected areas from slices containing transplanted graft were imaged.

For IHC of host-graft synapse evaluation, mouse anti-CACNA1s antibody (MAB427, Millipore, CA, USA) was used as the first antibody of the post-synaptic marker. Antigen retrieval was omitted in these samples in order to image GFP and tdTomato from the host bipolar cells and graft synaptic terminal CtBP2, respectively.

Image processing

Fiji (version 2.0.0-rc-65), an open source distribution of ImageJ (version 1.51s, NIH, USA) was used for image processing. IHC images were imported to Fiji, and 5 consecutive z-stack images from the upper edge of the sample were z-projected by averaging, to improve image quality and reduce noise. Protocols for DAPI, pre-synaptic and post-synaptic staining were optimized respectively as described below. More details including parameters of each functions are described in depth in Figs. S1-3.

[DAPI] (Fig. S1)

For processing of the DAPI channel, the "Subtract background" function was used to reduce the background signal, and a bandpass filter was applied for reducing small particle noises. To select the area with signal, "Robust Automatic Threshold Selection" was applied followed by the "Dilate" function to slightly enlarge the selection. Next, "Adjustable watershed" was applied to the image to separate nuclei that have been merged together. Then, "Analyze particle" function was used to select the threshold area and generate regions of interest (ROIs), which were later used on the original image to extract graphical information from the unaltered image.

[Pre-synaptic marker] (Fig. S2)

First, the "Subtract background" function was used to reduce the background signal, then a bandpass filter was applied to the images for reducing small particle noises. The image was then smoothed by applying the "Smoothing" function, to make the signal within each region more homogeneous. Next, images were roughly segmented using the "Find Maxima" function with the "Segmented Particle" option. This separates the entire image into smaller segments based on local maxima, allowing us to extract all the

regions regardless of signal intensity. Then, we performed a second "Find Maxima" function on each of the segments, but this time we used the "Maxima Within Tolerance" option for thresholding. The threshold area was then selected by the "Analyze Particle" function for later use as ROI. This sequential approach allowed us to have an adaptive threshold value based on the background intensity around each ROI.

[Post-synaptic marker] (Fig. S3)

A bandpass filter was applied to the images for reducing small particle noises. The post-synaptic marker mGluR6 has a punctate expression pattern in the ribbon synapse, and therefore we used the "Maximum filter" function to enhance the punctate signal. Then, images were processed the same way they were for the pre-synaptic marker. Briefly, images were segmented by the "Find Maxima" function with the "Segmented Particle" option, and adaptively thresholded in each segment, and ROIs were generated by the "Analyze Particle" function.

All generated ROIs were overlaid on the original z-projected image of each channel to extract 34 graphical parameters from each ROI of the unaltered image. Acquired ROI parameters were exported as a csv file for later use in the Naïve Bayes classifier.

All the processes described above were built into an ImageJ macro, so that images can be processed automatically, and multiple images can be processed in batch.

Training data of synapse and noise

The adult retina is organized into distinct layers, with photoreceptor/bipolar synapses located in the outer plexiform layer (OPL), an area that is clearly delineated by

photoreceptor cell and bipolar cell nuclei. We prepared images from postnatal day (P) 28 B6J mouse retina containing only the OPL or excluding the OPL as training data for *Ideal Synapse* and *Ideal Noise*. The OPL area was manually cropped assuming that signals from this area originate mostly from synapses. The complement of OPL was used as noise teacher data, on the assumption that there are almost no photoreceptor/bipolar synapses outside the OPL. Note that although we call it noise, we do not necessarily mean or assume that these are non-specific staining or artifacts. In fact, both pre- and post-synaptic markers are known to be present outside the OPL. For example, RIBEYE is present in the inner plexiform layer (IPL) on the axonal terminal of bipolar cells as well as in the OPL (tom Dieck and Brandstatter 2006); however, as its morphology and molecular component differs from that of the photoreceptor ribbon synapse (Heidelberger, Thoreson, and Witkovsky 2005), its staining pattern also differs. Thus, although both IPL and OPL synapses are visualized by RIBEYE immunostaining, a careful examination of their signal can distinguish them. Furthermore, the ribbon synapse of IPL and OPL can be distinguished by its post-synaptic marker, because the retinal ganglion cell does not express mGluR6 in IPL. We therefore called staining patterns that resemble the adult photoreceptor ribbon synapse *Ideal Synapse*, and any other signals *Ideal Noise*, regardless of whether those noise signals represent a physiological or functional signal or not.

Ideal Synapse and *Ideal Noise* data were segmented and thresholded, and graphical information of ROIs was extracted as described in Fig. 1 and Figs. S1-S3. We categorized the extracted parameters into three categories: *Signal*, *Morphology*, and

Geometry. *Signal* parameters include a series of measurements that represent the characteristics of staining signal including: *mean*, *median*, *mode*, *minimum*, *maximum*, *standard deviation*, *skewness*, and *kurtosis*. In addition to the raw value of these parameters, all the *Signal* parameters, except for *skewness* and *kurtosis*, were divided by a global background intensity to compensate for variance of IHC background intensity. The global background intensity was calculated from the pixel intensity of the entire image. The background was summarized as the peak value of the signal intensity distribution estimated using Kernel Density Estimation (KDE). Signals below the intensity of 8 were ignored in the peak estimation assuming they represent areas where there was no tissue. *Morphology* parameters include *perimeter*, *width*, *height*, *shape*, *major*, *minor*, *angle*, *AR*, *round*, *circularity*, *solidity*, *ferret*, *minferet*, *angle*, and *feret angle*. Perimeter represents the length of outer edge of the ROI. *Width* and *height* represent horizontal and vertical length of bounding box that can fit ROI. *Shape* parameter is our original parameter which is represented by $shape = \sqrt{\{XM - \left(BX - \frac{width}{2}\right)\}^2} + \sqrt{\{YM - \left(BY - \frac{height}{2}\right)\}^2}$ where XM and XM represents coordinates of brightness-weighted center of mass, and BX and BY represents coordinates of upper-left corner of rectangle. *Major* and *Minor* are the longer and shorter axis when the ROI was fitted with ellipsoid. *Angle* is the angle between the longer axis of the ROI and the horizontal line. *AR* is the aspect ratio of width and height of bounding box. *Feret* angle represents the angle of *feret* and *minferet* represents the longest and shortest diameter of the ROI. Geometrical parameters include the distance

between pre- and post-synaptic markers, the angle of the pair, the area of each synaptic marker, and the raw integrated density which represents area and intensity simultaneously.

Using the training data, we generated the Probability Density Functions (PDFs) of *Ideal Synapse* and *Ideal Noise* for each of the parameters (Supplemental Fig. 5). PDFs were estimated for each parameter from their histograms, either by Kernel Density Estimation (KDE), or by Bounded Density Estimation (BDE) for parameters that had a clear boundary.

Naïve Bayes classifier

The Naïve Bayes classifier is a simple but robust classifier algorithm, which employs the Bayes theorem to estimate the posterior probability using the prior probability and likelihood based on training data.

Naïve Bayes classifier used in QUANTOS can be represented as follows:

$$p(C_i|x_1 \dots x_n) = \frac{p(C_i)p(x_1 \dots x_n|C_i)}{p(x)} \qquad \text{(where } i = synapse\ or\ noise\text{)}$$

$p(C_i|x_1 \dots x_n)$ represents posterior probability of being either synapse or noise, given *n* different parameters *(x)*. $p(C_i)$ represents prior probability of synapse or noise, $p(x_1 \dots x_n|C_i)$ represents likelihood of synapse or noise under condition of parameters *x*, and $p(x)$ represents evidence.

[Prior probability]

Prior probability was estimated from marker density, on the assumption that the presence of more markers decreases the probability of correctly identifying synapses. We generated two sets of points randomly within a square area at different densities to simulate the behavior of non-specific pre- and post-synaptic makers. This simulation shows that the number of randomly generated pairs within a certain distance is proportional to the density of the markers (Fig. S4a). This can clearly be visualized in Fig. S4a, where the number of random pairs increases with marker density. The slope of the regression line, which we termed "random factor", is in a quadratic relationship with the maximum distance of pairs (Fig. S4c). Thus, the number of pairs formed by chance (i.e. random pairs) can be estimated from the marker density and the random factor with the following equation:

$$random\ pairs = (random\ factor) \times\ (density\ of\ pre) \times\ (density\ of\ post)$$

A 5 μm × 5 μm square area around each of the center coordinates markers was used for estimating pre- and post-synaptic marker density.

Having estimated the number of random pairs, the prior synapse probability is estimated as:

$$prior\ synapse\ probability = 0.5 \qquad (\text{if } random\ pairs < 2)$$

$$prior\ synapse\ probability = \frac{1}{random\ pairs} \qquad (\text{if } random\ pairs \geq 2)$$

The prior probability for noise is simply

$$prior\ noise\ probability = \ 1 - \ prior\ synapse\ probability$$

Thus, the priors for synapse and noise are equal if the number of markers is low, but the synapse prior decreases as the number or markers increases.

[Likelihood]

The likelihood is given by the Probability Density Function (PDF) of the *Ideal Synapse* and the *Ideal Noise* data. Pre- and post-synaptic markers are evaluated separately, and the total likelihood of synapse candidate pair is estimated by multiplying their individual likelihoods. Pre- and post-synaptic markers whose centroid coordinates were within 1.2 μm were assigned as possible synapse candidates. The distance threshold was decided based on the *Ideal Synapse* data set, where synapses were most often observed around 0.51 μm with a standard deviation of 0.17 μm. After selecting the synapse candidates, the Naïve Bayes classifier was used to estimate the likeliness of each synapse candidate being synapse or noise. Evidence is likewise calculated from the joint synapse and noise likelihoods, by the following:

$$(prior\ synapse\ probability\ \times\ likelihood\ of\ synapse) + (prior\ noise\ probability\ \times\ likelihood\ of\ noise)$$

Analysis of rd1 mice after miPSC-retina transplantation

Unlike postnatal development of the B6J mouse, the number of transplanted photoreceptors is not homogenous among samples. Therefore, the numbers of photoreceptors were quantified in transplanted samples to estimate the number of synapses per photoreceptor. Transplanted photoreceptors can be identified by their nuclei shape, characteristic of photoreceptor cells, and by the formation of dome-like

structures called rosettes. For quantification of photoreceptors, the area of rosette forming cells was manually selected in each image, then the number of DAPI ROIs contained in that area was analyzed using the protocol for DAPI analysis described above in the “Image Processing” section.

Average synapse

All detected synapses were individually cropped to a 4.34 by 4.34 μm square, with the center coordinates of the synapse in the center of the square. Ribbon synapses can be formed at various angles (Fig. 2d) and thus images were rotated to align the center coordinates of pre- and post-synaptic markers, using the angle of the line connecting the pre- and post-synaptic markers. Then all synapses from each postnatal day and each rearing condition were averaged. For analysis of average synapse data, we used “Radial Profile” of ImageJ Fiji, which exports the intensity along the distance from the center coordinates. The center coordinates of averaged images were estimated using the “Find Maxima” function for both pre- and post-synaptic markers.

Micro-electroretinography (mERG)

The mERG was conducted using the multi-electrode array (MEA) recording system (USB-MEA60-Up-System, MultiChannel Systems, Germany) with the standard 8x8 probe (60MEA200/30iR-Ti-gr) as previously described(Iraha et al. 2018). In order to distinguish the effects of prolonged dark adaptation from dark rearing, mice reared under LD and LL conditions were dark adapted for 24 hours prior to the recording, as

long dark adaptation (6 to 24 hours) can significantly reduce the b-wave amplitude(Li, Fang, and Yu 2016). P14 B6J mice were deeply anesthetized with sevoflurane inhalation, followed immediately by decerebration and harvest of retinas. After removal of the vitreous body, retinas were mounted on electrodes with the ganglion cell side down and constantly supplied with warmed (35 ± 0.5°C), carbonated (95% O_2 and 5% CO_2) Ames' medium (A1420, Sigma-Aldrich) perfused at 3-3.5 mL/min. Opsinamide (10 μM; AA92593, Sigma-Aldrich) was added in the perfusion medium to suppress the melanopsin-driven RGC light responses during recording. Retinas were allowed to recover in the MEA chamber for at least 20 min before recording. Field potentials to full-field white light stimuli were recorded at 20 kHz. The 10 ms full-field light stimulus was generated using a white LED source with an irradiance of 10.56 log photons/cm^2/s at the focal plane of the electrodes, which approximated the low mesopic range of mature wildtype mouse vision. All of the above procedures were conducted under dim LED light with a peak wavelength at 690 nm.

mERG traces were processed and analyzed in R(RC Team - Austria: R Foundation for Statistical Computing Google …2017, n.d.). A band-pass Butterworth filter (1 to 50 Hz) was applied to traces to remove low frequency fluctuations and high frequency jitter. Local minima within 55 ms from light stimulation were flagged as a-wave, and local maxima within 150 ms from light stimulation were flagged as b-wave. The a-wave amplitude was calculated from the baseline, and the b-wave amplitude was calculated from the a-wave, or from the baseline when the a-wave was not detected. Replicates from three repeated stimulations were averaged.

Statistical analysis

We used full Bayesian statistical inference with MCMC sampling for statistical modeling. Bayesian inference was implemented in Rstan (Stan Development Team. 2017. *RStan: the R interface to Stan*. R package version 2.16.2. http://mc-stan.org). We estimated population effects, such as the effect of light, individual differences, as well as experimental variation.

Posterior distribution of parameters of interest, which show the most likely values given the data, are shown with 89% confidence intervals. When the difference between conditions is of interest, we show the difference of posterior distributions expressly, as posterior distributions may be correlated or anticorrelated. When the 89% confidence interval of difference of posterior distributions does not cross over zero, estimated parameters are considered different.

[Developmental B6J mouse analysis]

We parameterized developmental synaptogenesis with a modified (Gompertz) growth curve (Zwietering et al. 1990), which is defined by three parameters describing the onset of synaptogenesis (λ), the maximum rate of synaptogenesis (μ) and the maximum capacity of synapse (A). Acquired data was analyzed with the following multilevel model:

$$y_i \sim Poisson(\Lambda_{mouse})$$

$$\Lambda_{mouse} \sim Gamma(\Lambda_{condition,day}, \beta)$$

$$\Lambda_{condition,day} \sim Gompertz(A_{condition}, \mu_{condition}, \lambda_{condition}, day)$$

Each observation y_i is a count data, so we assumed a Poisson distribution with a mean Λ_{mouse}, representing the average number of synapses for the sampled mouse. We assumed a Gamma distribution for mice sampled on the same postnatal days, as the average number of synapses should be a positive number. The expected number of synapses is given by the Gompertz growth curve given the rearing condition (DD or LD) and postnatal day.

[mERG analysis]

B-wave amplitude was analyzed with a multilevel generalized linear model using the Gamma distribution as likelihood, as b-wave amplitude is always a positive value and data was spread with a long tail towards larger values.

$$A_n \sim Gamma(\mu_n, \sigma_n) \qquad n = 1, \dots, N$$

where A_n is the b-wave amplitude of the n-th observation, μ is the mean, and σ represents the standard deviation. We parameterized with the mean and standard deviation rather than the shape and rate parameters, in order to place informative priors and to make the interpretation more intuitive. The different rearing conditions and the animals from which samples were obtained were used as predictors with the exponential link function.

$$\mu = \exp\left(a_0 + a_{condition} + a_{mouse}\right)$$

$$\sigma = \exp\left(b_0 + b_{condition} + b_{mouse}\right)$$

[Synapse number after transplantation]

The number of synapses per photoreceptor cell on post-transplantation samples was compared using the Student-t distribution for robust Bayesian estimation assuming equal variance between conditions. Thus each observation (number of synapses per photoreceptor cells) y_i is distributed as

$$y_i \sim Student\_t(\upsilon, \mu_i, \sigma)$$

where υ is the normality parameter, μ is the mean, and σ is the standard deviation. The different rearing conditions and the animals from which samples were obtained were used as predictors.

$$\mu_i = a_o + a_{condition} + a_{mouse}$$

[ROC analysis]

Ground truths for P14 and P28 samples were generated by careful classification by an expert observer. ROC curve analysis was conducted using the "pROC" package in R(Robin et al. 2011). The ROC curve was drawn in reference to the ground truth to evaluate the sensitivity and specificity of QUANTOS.

Acknowledgements

We would like to thank Genshiro A Sunagawa for his valuable comments and discussion on the statistical analysis and development of QUANTOS; Jutaro Nakamura for his advice and insight on ERG recordings; and Sugury Yamasaki for advice on retinal organoid culture and immunostaining.

This study was supported by AMED under grant number 18bm0204002h0006 awarded to M.T. and 2018 JRPS grant awarded to T.M.

Author Contributions

R.A., T.M., M.T., and M.M. conceptualized the study, R.A. and T.M. developed QUANTOS and conducted the statistical analysis, R.A. conducted immunohistochemistry, R.A., M.M. performed subretinal transplantation, H-Y.T. conducted electrophysiology, T.H. maintained and differentiated mES/iPSC retina, J.S. cared for animals and assisted on transplantation, M.T., S.Y., oversaw the study, and R.A., T.M., H-Y.T., and M.M. wrote the manuscript with input from all authors.

Conflict of Interest

The authors declare no conflicts of interest.

References

Akimoto, M, H Cheng, D Zhu, J A Brzezinski, R Khanna, E Filippova, E C Oh, et al. 2006. "Targeting of GFP to Newborn Rods by Nrl Promoter and Temporal Expression Profiling of Flow-Sorted Photoreceptors." *Proc Natl Acad Sci U S A* 103 (10): 3890–95. doi:10.1073/pnas.0508214103.

Anastassov, Ivan A, Weiwei Wang, and Felice A Dunn. 2017. "Synaptogenesis and Synaptic Protein Localization in the Postnatal Development of Rod Bipolar Cell Dendrites in Mouse Retina." *J Comp Neurol* 289 (June): 27019. doi:10.1002/cne.24251.

Assawachananont, J, M Mandai, S Okamoto, C Yamada, M Eiraku, S Yonemura, Y Sasai, and M Takahashi. 2014. "Transplantation of Embryonic and Induced Pluripotent Stem Cell-Derived 3D Retinal Sheets Into Retinal Degenerative Mice." *Stem Cell Reports* 2 (5): 662–74. doi:10.1016/j.stemcr.2014.03.011.

Barnea-Cramer, Alona O, Wei Wang, Shi-Jiang Lu, Mandeep S Singh, Chenmei Luo, Hongguang Huo, Michelle E McClements, Alun R Barnard, Robert E MacLaren, and Robert Lanza. 2016. "Function of Human Pluripotent Stem Cell-Derived Photoreceptor Progenitors in Blind Mice.." *Sci Rep* 6 (1): 29784. doi:10.1038/srep29784.

Blanks, J C, A M Adinolfi, and R N Lolley. 1974. "Photoreceptor Degeneration and Synaptogenesis in Retinal-Degenerative (Rd) Mice.." *J Comp Neurol* 156 (1): 95–106. doi:10.1002/cne.901560108.

Dana, Hod, Tsai-Wen Chen, Amy Hu, Brenda C Shields, Caiying Guo, Loren L Looger,

Douglas S Kim, and Karel Svoboda. 2014. “Thy1-GCaMP6 Transgenic Mice for Neuronal Population Imaging in Vivo..” Edited by Benjamin Arenkiel. *PLoS One* 9 (9). Public Library of Science: e108697. doi:10.1371/journal.pone.0108697.

DiStefano, Tyler, Holly Yu Chen, Christopher Panebianco, Koray Dogan Kaya, Matthew J Brooks, Linn Gieser, Nicole Y Morgan, Tom Pohida, and Anand Swaroop. 2018. “Accelerated and Improved Differentiation of Retinal Organoids From Pluripotent Stem Cells in Rotating-Wall Vessel Bioreactors..” *Stem Cell Reports* 10 (1): 300–313. doi:10.1016/j.stemcr.2017.11.001.

Dominic M Ippolito, Cagla Eroglu. 2010. “Quantifying Synapses: an Immunocytochemistry-Based Assay to Quantify Synapse Number.” *J Vis Exp*, no. 45. MyJoVE Corporation. doi:10.3791/2270.

Dunn, Felice A, Luca Della Santina, Edward D Parker, and Rachel O L Wong. 2013. “Sensory Experience Shapes the Development of the Visual System's First Synapse..” *Neuron* 80 (5): 1159–66. doi:10.1016/j.neuron.2013.09.024.

Fantuzzo, J A, V R Mirabella, A H Hamod, R P Hart, J D Zahn, and Z P Pang. 2017. “Intellicount: High-Throughput Quantification of Fluorescent Synaptic Protein Puncta by Machine Learning.” *eNeuro* 4 (6). doi:10.1523/ENEURO.0219-17.2017.

Geinisman, Y, H J G Gundersen, E Van Der Zee, and M J West. 1996. “Unbiased Stereological Estimation of the Total Number of Synapses in a Brain Region.” *Journal of Neurocytology* 25 (1). Kluwer Academic Publishers: 805–19. doi:10.1007/BF02284843.

Glynn, Marian W, and A Kimberley McAllister. 2006. “Immunocytochemistry and

Quantification of Protein Colocalization in Cultured Neurons." *Nature Protocols* 1 (3). Nature Publishing Group: 1287–96. doi:10.1038/nprot.2006.220.

Heidelberger, Ruth, Wallace B Thoreson, and Paul Witkovsky. 2005. "Synaptic Transmission at Retinal Ribbon Synapses." *Prog Retin Eye Res* 24 (6): 682–720. doi:10.1016/j.preteyeres.2005.04.002.

Homma, K, S Okamoto, M Mandai, N Gotoh, H K Rajasimha, Y S Chang, S Chen, et al. 2013. "Developing Rods Transplanted Into the Degenerating Retina of Crx-Knockout Mice Exhibit Neural Activity Similar to Native Photoreceptors." *Stem Cells* 31 (6): 1149–59. doi:10.1002/stem.1372.

Iraha, Satoshi, Hung-Ya Tu, Suguru Yamasaki, Takahiro Kagawa, Motohito Goto, Riichi Takahashi, Takehito Watanabe, et al. 2018. "Establishment of Immunodeficient Retinal Degeneration Model Mice and Functional Maturation of Human ESC-Derived Retinal Sheets After Transplantation." *Stem Cell Reports* 10 (3). Cell Press: 1059–74. doi:10.1016/j.stemcr.2018.01.032.

Jorstad, N L, M S Wilken, W N Grimes, S G Wohl, L S VandenBosch, T Yoshimatsu, R O Wong, F Rieke, and T A Reh. 2017. "Stimulation of Functional Neuronal Regeneration From Muller Glia in Adult Mice." *Nature* 548 (7665). Nature Publishing Group: 103–7. doi:10.1038/nature23283.

Li, D, Q Fang, and H Yu. 2016. "The Shift of ERG B-Wave Induced by Hours' Dark Exposure in Rodents." *PLoS One* 11 (8): e0161010. doi:10.1371/journal.pone.0161010.

Lowel, S, and W Singer. 1992. "Selection of Intrinsic Horizontal Connections in the

Visual Cortex by Correlated Neuronal Activity." *Science* 255 (5041): 209–12.

Mandai, M, M Fujii, T Hashiguchi, G A Sunagawa, S Ito, J Sun, J Kaneko, J Sho, C Yamada, and M Takahashi. 2017. "iPSC-Derived Retina Transplants Improve Vision in Rd1 End-Stage Retinal-Degeneration Mice." *Stem Cell Reports* 8 (1): 69–83. doi:10.1016/j.stemcr.2016.12.008.

Matthews, G, and P Fuchs. 2010. "The Diverse Roles of Ribbon Synapses in Sensory Neurotransmission." *Nat Rev Neurosci* 11 (12): 812–22. doi:10.1038/nrn2924.

RC Team - Austria: R Foundation for Statistical Computing Google …, 2017. n.d. *R: a Language and Environment for Statistical Computing. Vienna; 2014*.

Regus-Leidig, H, S tom Dieck, D Specht, L Meyer, and J H Brandstatter. 2009. "Early Steps in the Assembly of Photoreceptor Ribbon Synapses in the Mouse Retina: the Involvement of Precursor Spheres" 512 (6): 814–24. doi:10.1002/cne.21915.

Ribic, A, X Liu, M C Crair, and T Biederer. 2014. "Structural Organization and Function of Mouse Photoreceptor Ribbon Synapses Involve the Immunoglobulin Protein Synaptic Cell Adhesion Molecule 1." *J Comp Neurol* 522 (4): 900–920. doi:10.1002/cne.23452.

Robin, Xavier, Natacha Turck, Alexandre Hainard, Natalia Tiberti, Frédérique Lisacek, Jean-Charles Sanchez, and Markus Müller. 2011. "pROC: an Open-Source Package for R and S+ to Analyze and Compare ROC Curves." *BMC Bioinformatics* 12 (1). BioMed Central: 77. doi:10.1186/1471-2105-12-77.

Silver, Michael A, and Michael P Stryker. 2000. "A Method for Measuring Colocalization of Presynaptic Markers with Anatomically Labeled Axons Using

Double Label Immunofluorescence and Confocal Microscopy." *Journal of Neuroscience Methods* 94 (2). Elsevier: 205–15. doi:10.1016/S0165-0270(99)00145-4.

Singh, M S, P Charbel Issa, R Butler, C Martin, D M Lipinski, S Sekaran, A R Barnard, and R E MacLaren. 2013. "Reversal of End-Stage Retinal Degeneration and Restoration of Visual Function by Photoreceptor Transplantation." *Proc Natl Acad Sci U S A* 110 (3): 1101–6. doi:10.1073/pnas.1119416110.

Spiwoks-Becker, I, M Glas, I Lasarzik, and L Vollrath. 2004. "Mouse Photoreceptor Synaptic Ribbons Lose and Regain Material in Response to Illumination Changes." *Eur J Neurosci* 19 (6): 1559–71. doi:10.1111/j.1460-9568.2004.03198.x.

Sterling, P, and G Matthews. 2005. "Structure and Function of Ribbon Synapses." *Trends Neurosci* 28 (1): 20–29. doi:10.1016/j.tins.2004.11.009.

Tian, Ning. 2004. "Visual Experience and Maturation of Retinal Synaptic Pathways.." *Vision Res* 44 (28): 3307–16. doi:10.1016/j.visres.2004.07.041.

tom Dieck, S, and J H Brandstatter. 2006. "Ribbon Synapses of the Retina." *Cell Tissue Res* 326 (2): 339–46. doi:10.1007/s00441-006-0234-0.

tom Dieck, Susanne, Wilko D Altrock, Michael M Kessels, Britta Qualmann, Hanna Regus, Dana Brauner, Anna Fejtová, Oliver Bracko, Eckart D Gundelfinger, and Johann H Brandstätter. 2005. "Molecular Dissection of the Photoreceptor Ribbon Synapse: Physical Interaction of Bassoon and RIBEYE Is Essential for the Assembly of the Ribbon Complex.." *J Cell Biol* 168 (5): 825–36. doi:10.1083/jcb.200408157.

Vardi, N, R Duvoisin, G Wu, and P Sterling. 2000. “Localization of mGluR6 to Dendrites of on Bipolar Cells in Primate Retina.” *J Comp Neurol* 423 (3): 402–12.

Wu, M L, and C C Chiao. 2007. “Light Deprivation Delays Morphological Differentiation of Bipolar Cells in the Rabbit Retina.” *Brain Res* 1170 (September): 13–19. doi:10.1016/j.brainres.2007.06.091.

Yao, Kai, Suo Qiu, Yanbin V Wang, Silvia J H Park, Ethan J Mohns, Bhupesh Mehta, Xinran Liu, et al. 2018. “Restoration of Vision After De Novo Genesis of Rod Photoreceptors in Mammalian Retinas..” *Nature* 560 (7719). Nature Publishing Group: 484–88. doi:10.1038/s41586-018-0425-3.

Zwietering, M H, I Jongenburger, F M Rombouts, and K van 't Riet. 1990. “Modeling of the Bacterial Growth Curve..” *Applied and Environmental Microbiology* 56 (6). American Society for Microbiology: 1875–81.

Figure Legends

Fig. 1: Overview of QUANTOS, a synapse evaluation method using a Naïve Bayes classifier

(a) IHC Images from P28 B6J mice were used as training data for *Ideal Synapse* and *Ideal Noise*. The OPL area was manually isolated to train the *Ideal Synapse*, and the area outside the OPL was used to train the *Ideal Noise*. Scale bar = 4 μm.

(b) Examples of the various IHC images used in the present study. Scale bar = 4 μm.

(c) IHC images were processed by custom made ImageJ Fiji macros. IHC images were segmented, and thresholded using the background intensity of each segment. The thresholded areas were then overlaid on the original IHC image to extract graphical parameters from ROIs. Details of image processing steps for DAPI, RIBEYE, and mGluR6 are described in

Figs. S1-S3.

(d) The extracted parameters were used to generate PDFs for *Ideal Synapse* and *Ideal Noise*. The PDFs used in QUANTOS are shown in Fig. S5.

(e) Pre- and post-synaptic markers within 1.2 μm of each other (distance from center of mass) were considered as synapse candidates. Likelihoods of being synapse or noise were then estimated by referring to PDFs of *Ideal Synapse* and *Ideal Noise*.

(f) Posterior synapse probability of candidate markers is estimated from the prior probability of synapse (Fig. S4), and the total synapse likelihood of the 34 parameters. Synapse candidates with more than 50% of posterior probability were classified as synapse.

IHC, immunohistochemistry; IPL, inner plexiform layer; OPL, outer plexiform layer; ONL, outer nuclear layer; ROIs, regions of interest; PDF, probability density function.

Fig. 2: Sensitivity and specificity of QUANTOS.

(a-b) ROC curves of classifiers using different combinations of parameters on P14 (a) and P28 (b) samples. Dots indicate the results of manual counts by different observers.

(c) Histogram of the distances between pre- and post-synaptic markers.

(d) Histogram of the angles between pre- and post-synaptic markers.

(e) Example of QUANTOS on an IHC image of B6J P28 mouse. Yellow circles indicate synapses detected by QUANTOS.

(e') Magnified view of the magenta square in (e).

(f) Pre- (left column) and post-synaptic marker (right column) coordinates detected by QUANTOS. Each row shows the synapse candidates, i.e., candidates with high synapse likelihood given different parameters. White dots represent all the markers detected in the Image Processing, and gray dots represents all the synapse candidates (pre- and post-synaptic markers within 1.2 μm), and colored dots represent the synapse candidates with higher likelihood of synapse than noise for different parameters. "score_total" represents the combined likelihoods of all parameters and pre- and post-synaptic markers. "naïve_bayes" shows the marker pairs identified as synapses by QUANTOS, which are obtained from "score_total" by taking into account the prior probability of synapse.

ROC, receiver operation characteristics.

Fig. 3: Qualitative and quantitative evaluation of developmental synaptogenesis by QUANTOS in mice reared in DD and LD conditions.

(a) IHC images of B6J mice on different postnatal days. RIBEYE is the pre-synaptic marker expressed in photoreceptors and mGluR6 is the post-synaptic maker expressed in bipolar cells. Scale bar = 10 μm.

(b) Result of synapse quantification of postnatal B6J reared under LD and DD conditions. Dots indicate the number of synapses detected in each IHC image. The dark color-filled area shows the estimated range of mean number of synapses, and the pale color-filled area represents the estimated range of synapse numbers from each IHC image. (n=3 for P7, P10, P35 and n=4 for P14, 21, 28 samples. 3-4 replicates were taken from each mouse as indicated by the shape of markers.)

(c) Posterior distributions of modified Gompertz model parameters with 89% confidence interval.

(d) Difference of posterior distributions of parameters between LD and DD conditions.

(e) Developmental synaptogenesis was parameterized with the modified Gompertz's growth curve which has three parameters; the maximum number of synapses (A), maximum rate of synaptogenesis (μ_M), and the onset of synaptogenesis (λ).

(f) 2D histograms of all synapse candidates on different postnatal days, with log synapse likelihood on the x axis, and log noise likelihood on the y axis. Synapse candidates on the left-upper side are more likely to be noise, and the ones on the right-lower side are more likely to be synapses.

(g) All synapses detected by QUANTOS were averaged to visualize the characteristics of synapses on different postnatal days and different rearing conditions.

(h) Radial profile plots of averaged synapses. The plots show the signal intensity in relation to the center coordinates of pre- and post-synaptic markers. Colors indicate different postnatal days.

IHC, immunohistochemistry; INL, inner nuclear layer; OPL, outer plexiform layer, ONL; outer nuclear layer; LD, cyclic light; DD, constant dark; P, postnatal day; HDI, high density interval.

Fig. 4: Rearing light conditions alter developmental synaptic function.

(a) An example of mERG recording. Retinas flat-mounted on the 60-channel probe were stimulated with a mesopic light pulse. The red box is a magnified view of a single channel recording trace, showing a typical waveform with an a-wave and a b-wave.

(b) Upper panels show histograms of b-wave amplitudes of wildtype P14 mice reared under different light conditions (n=5 for DD and n=4 for LD and LL) and the posterior predictive check of the statistical model used to analyze the data is shown in the lower panels.

(c) Posterior distributions of mean b-wave amplitude .

(d) Estimated impact of light on mean b-wave amplitudes.

(e) Posterior distributions b-wave amplitude SD.

(f) Estimated impact of light on SD of mean b-wave amplitudes.

mERG, micro electroretinography; HDI, high density interval; SD, standard deviation.

Fig. 5: QUANTOS evaluation of synapses during photoreceptor degeneration.

(a) IHC images of *rd1* mice retinas on different postnatal days. Scale bar = 10 μm.

(b) The number of synapses detected on different postnatal days in *rd1* mice, accompanied by B6J LD data for comparison. (n=3 for each postnatal day of *rd1*. 3-4 replicates were taken from each mouse as indicated by the shape of markers.)

(c) Number of photoreceptor cells estimated form IHC images on different postnatal days of *rd1* mice retinas, accompanied by B6J data for comparison.

(d) 2D histograms of all synapse candidates on different postnatal days, with log synapse likelihood on the x axis, and log noise likelihood on the y axis.

(e) Averaged images of all synapses detected by QUANTOS show the characteristics of synapses on different postnatal days and different rearing conditions. Scale bar = 0.5 μm

(f) Radial profile plot of averaged synapses. This plot shows the intensity of signals in relation to the center coordinates of pre- and post-synaptic markers. Colors indicate different postnatal days.

IHC, immunohistochemistry; INL, inner nuclear layer; OPL, outer plexiform layer, ONL; outer nuclear layer; SD, standard deviation.

Fig. 6: QUANTOS detects *de novo* synapses after miPSC-retina transplantation and shows that light enhances synaptogenesis.

(a-c) Example IHC images of *rd1* mice after miPSC-retina transplantation on PT 14, 30, 60. Bottom panels show magnified images of some synapse candidates. Scale bar = 10 μm

(d) Number of synapses of *rd1* mice before and after transplantation of miPSC-retina under different rearing light conditions. (5 and 4 retinal organoids were sampled for *in vitro* dd25 and dd36, respectively. n= 4 for PT10 LD, n=3 for PT14 LD, n=2 for PT14 DD, n=5 for PT30 LD, n=4 for PT30 DD, n=5 for PT60 LD, n=4 for PT60 DD. 3-4 replicates were taken from each mouse as indicated by the shape of markers.)

(e) Estimated mean number of synapses per photoreceptor on PT 14, 30 and 60.

(f) Difference of estimated mean number of synapses per photoreceptor between DD and LD.

(g) 2D histograms of all synapse candidates on different postnatal days, with log synapse likelihood on the x axis, and log noise likelihood on the y axis.

(h) Average synapse of *rd1* mice before and after miPSC-retina transplantation. All synapses detected by QUANTOS were averaged from different time points, respectively. Scale bar = 0.5 μm

(i) Radial profile plot of averaged synapses. This plot shows the intensity of signals in relation to the center coordinates of pre- and post-synaptic markers. Colors indicate different postnatal days.

Data of B6J is presented together for comparison.

IHC, immunohistochemistry; PT, post-transplantation day; LD, cyclic light; DD, constant dark; dd, differentiation day; INL, inner nuclear layer; OPL, outer plexiform layer, ONL; outer nuclear layer.

Fig. 7: miPSC-retina can form *de novo* host-graft synapses and have the potential to reconstruct the OPL.

(a) An IHC image of *rd1* mouse 60 days after miPSC-retina transplantation with a substantial OPL-like structure. Transplanted cells lined up horizontally and formed an ONL-like structure with synapses at a similar density to wildtype OPL. White arrows, magnified on the right column, show some of the synapses with mature morphology.

(b) IHC image of Ctbp2-tdTomato transgenic mESC-retina transplanted to L7-GFP/*rd1* mouse. Host bipolar cells expressing GFP extend their dendrites to transplanted cells, making synaptic contact on their dendritic tips. The yellow box area is magnified (b'-b''), showing the post-synaptic marker cacna1s localizing to the dendritic tip of host bipolar cell, accompanied by graft CtBP2-tdTomato.

IHC, immunohistochemistry; ONL, outer nuclear layer.

Fig. 8: QUANTOS can compare the relative maturation of synapses formed during development, degeneration, and regeneration of the retina.

(a-c) 2D histograms showing the log likelihood of mature synapse on the x axis, and the log likelihood of immature synapse on the y axis.

(a) Synapse maturation of B6J mice reared under LD or DD conditions with representative IHC images of synapses from P10 DD and P28 LD.

(b) Synapse maturation of *rd1* mice with representative IHC images of mature and immature synapses are presented as examples.

(c) Synapse maturation of *rd1* mice after miPSC-retina transplantation with representative IHC images of mature and immature synapses.

(d) Synapses of *rd1* mice after miPSC-retina transplantation with pre- and post-synaptic maker log mature/immature likelihoods displayed separately.

IHC, immunohistochemistry; LD, cyclic light; DD, constant dark.

Figs. S1, S2, S3 describe image processing protocols for DAPI, RIBEYE, and mGluR6 channel, respectively. Immunostaining samples were imaged with a confocal microscope and 5 sequential z-stack images were projected on the z axis, and processed as described in the figure. After generating ROIs, the following graphical parameters were exported using the "Measure" function of ImageJ Fiji: *Area*, *Mean*, *StdDev*, *Mode*, *Min*, *Max*, *X*, *Y*, *XM*, *YM*, *Perim*, *BX*, *BY*, *Width*, *Height*, *Major*, *Minor*, *Angle*, *Circ*, *Feret*, *IntDen*, *Median*, *Skew*, *Kurt*, *RawIntDen*, *FeretX*, *FeretY*, *FeretAngle*, *MinFeret*, *AR*, *Round*, *Solidity*.

Fig. S4: Estimation of marker density.

(a) Relationship between pre-synaptic marker density, post-synaptic marker density and the number of pairs when the maximum distance of pairs is 1 μm.

(b) Modified figure of (a) with the y axis divided by post-synaptic density.

(c) (b) with different maximum distance of pairs.

Fig. S5: Probability density functions of parameters.

PDFs were generated by Ideal Synapse and Ideal Noise data. Likelihoods based on each PDF were used upon estimating the posterior probability of synapse for each synapse candidate.

PDF, probability density function.

Fig. 1

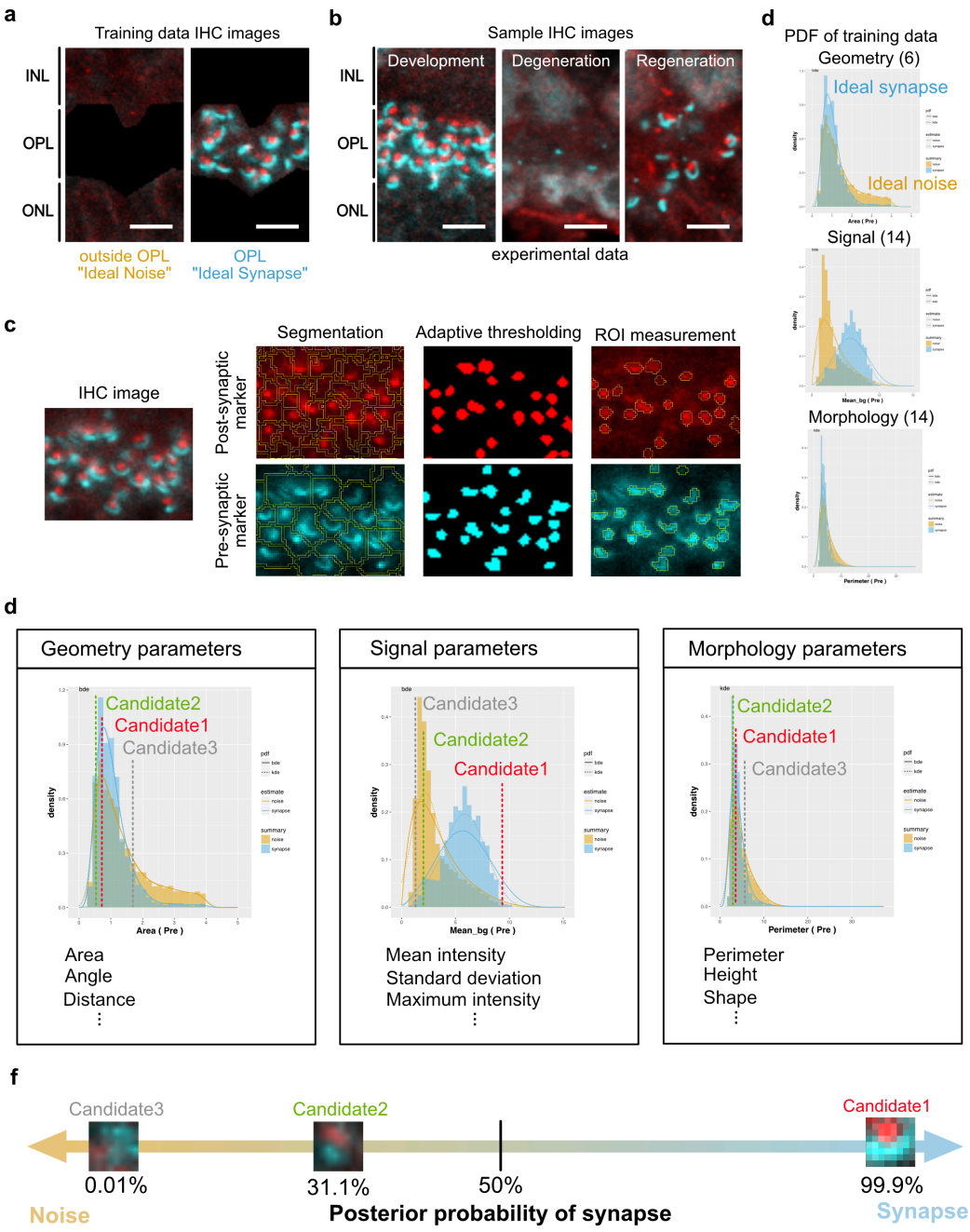
a
Training data IHC images
INL
OPL
ONL
outside OPL
"Ideal Noise"
OPL
"Ideal Synapse"
b
Sample IHC images
Development
Degeneration
Regeneration
experimental data
d
PDF of training data
Geometry (6)
Ideal synapse
Ideal noise
Signal (14)
Morphology (14)
c
IHC image
Segmentation
Adaptive thresholding
ROI measurement
Post-synaptic marker
Pre-synaptic marker
d
Geometry parameters
Candidate2
Candidate1
Candidate3
Area
Angle
Distance
Signal parameters
Mean intensity
Standard deviation
Maximum intensity
Morphology parameters
Perimeter
Height
Shape
f
Candidate3
Candidate2
Candidate1
0.01%
31.1%
50%
99.9%
Noise
Posterior probability of synapse
Synapse

Fig. 2

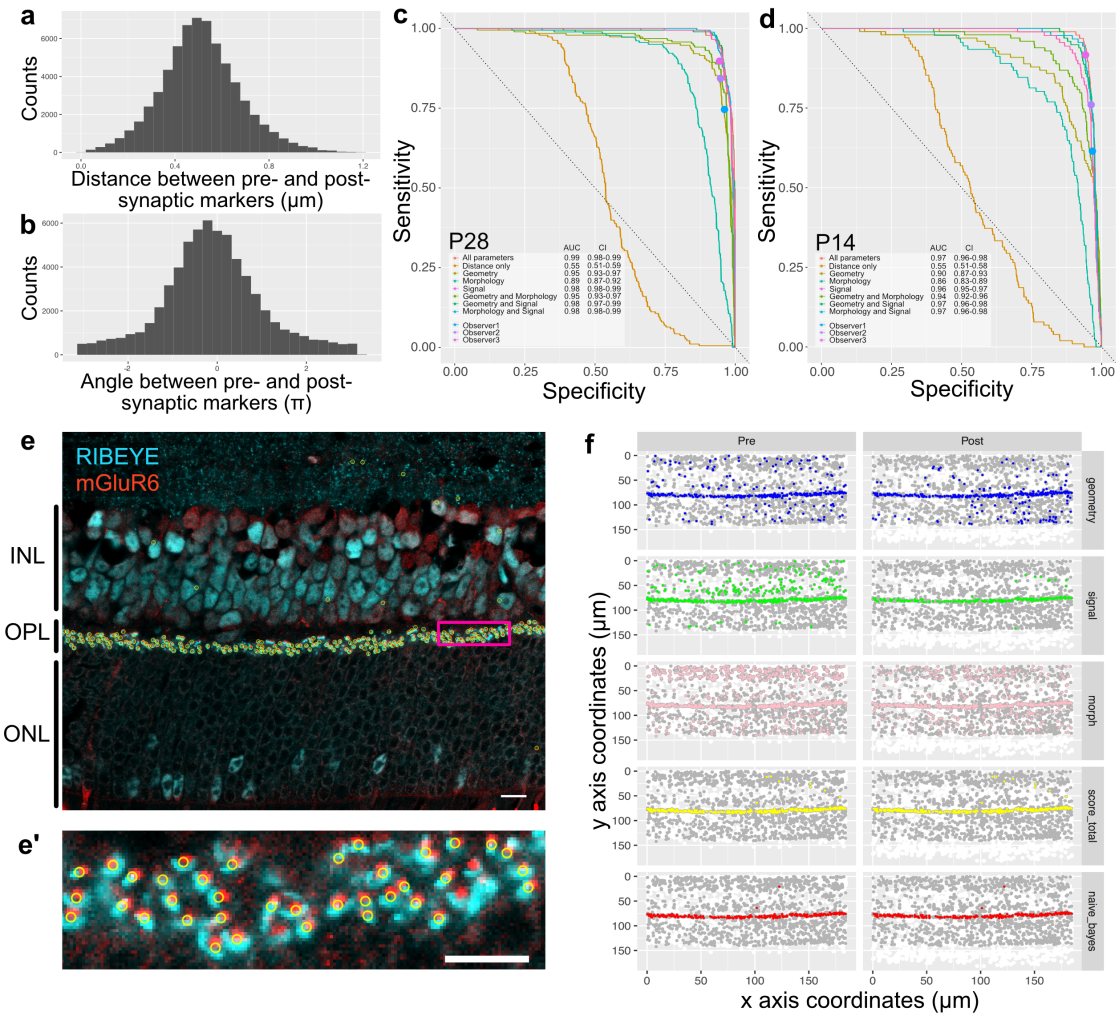
a
Counts
Distance between pre- and post-synaptic markers (µm)
b
Counts
Angle between pre- and post-synaptic markers (π)
c
Sensitivity
Specificity
P28
AUC CI
All parameters 0.99 0.98-0.99
Distance only 0.55 0.51-0.59
Geometry 0.95 0.93-0.97
Morphology 0.89 0.87-0.92
Signal 0.98 0.98-0.99
Geometry and Morphology 0.95 0.93-0.97
Geometry and Signal 0.98 0.97-0.99
Morphology and Signal 0.98 0.98-0.99
Observer1
Observer2
Observer3
d
Sensitivity
Specificity
P14
AUC CI
All parameters 0.97 0.96-0.98
Distance only 0.55 0.51-0.58
Geometry 0.90 0.87-0.93
Morphology 0.86 0.83-0.89
Signal 0.96 0.95-0.97
Geometry and Morphology 0.94 0.92-0.96
Geometry and Signal 0.97 0.96-0.98
Morphology and Signal 0.97 0.96-0.98
Observer1
Observer2
Observer3
e
RIBEYE
mGluR6
INL
OPL
ONL
e'
f
Pre
Post
geometry
signal
morph
score_total
naive_bayes
y axis coordinates (µm)
x axis coordinates (µm)

Fig. 3

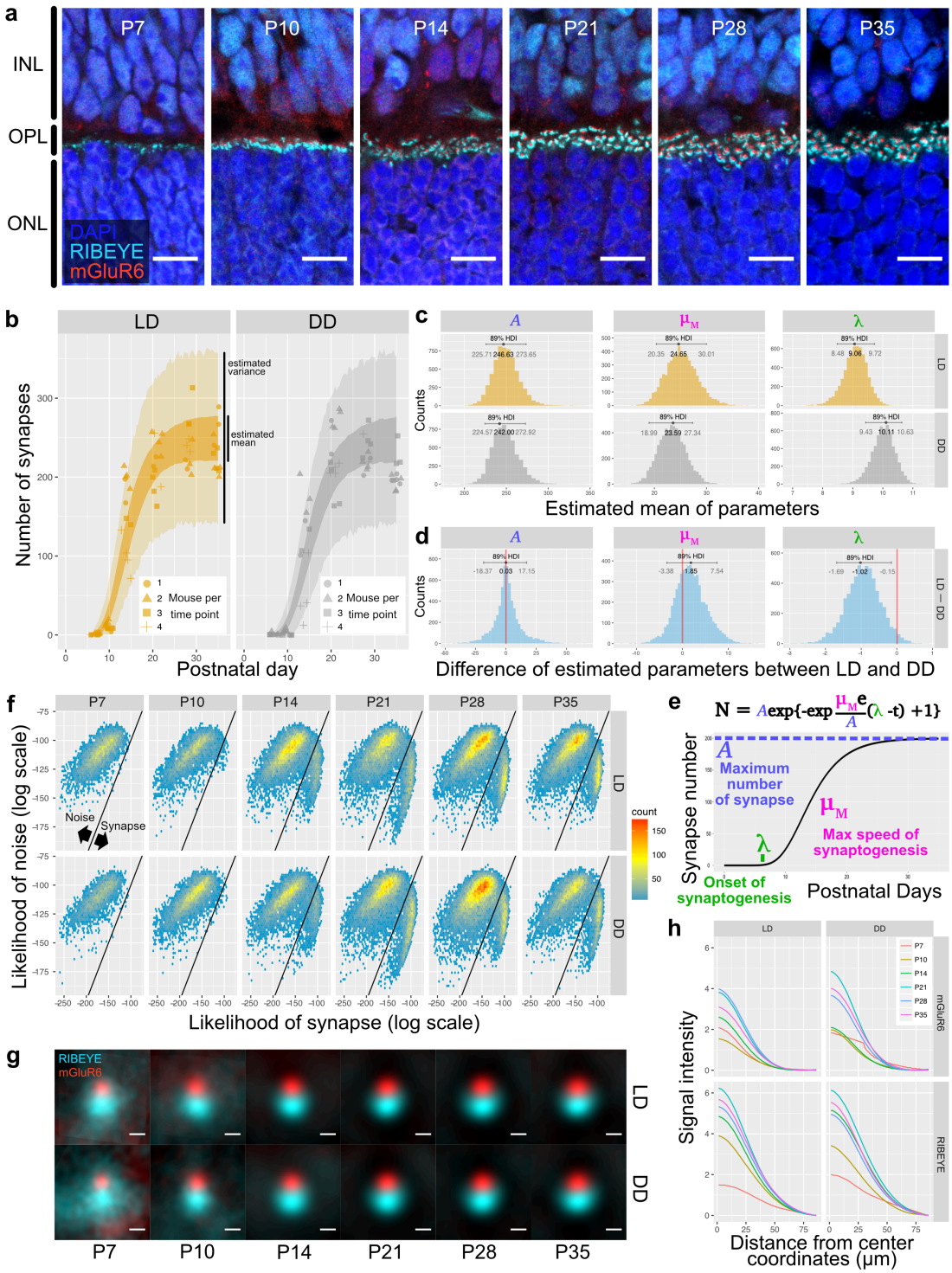
a
INL
OPL
ONL
P7
P10
P14
P21
P28
P35
DAPI
RIBEYE
mGluR6
b
LD
DD
estimated variance
estimated mean
Number of synapses
1
2 Mouse per
3 time point
4
Postnatal day
c
A
μM
λ
89% HDI
Counts
Estimated mean of parameters
d
Difference of estimated parameters between LD and DD
LD − DD
e
N = Aexp{-exp μM/A e(λ -t) +1}
Synapse number
Maximum number of synapse
Max speed of synaptogenesis
Onset of synaptogenesis
Postnatal Days
f
Likelihood of noise (log scale)
Noise
Synapse
count
Likelihood of synapse (log scale)
g
RIBEYE
mGluR6
h
Signal intensity
Distance from center coordinates (μm)

Fig. 4

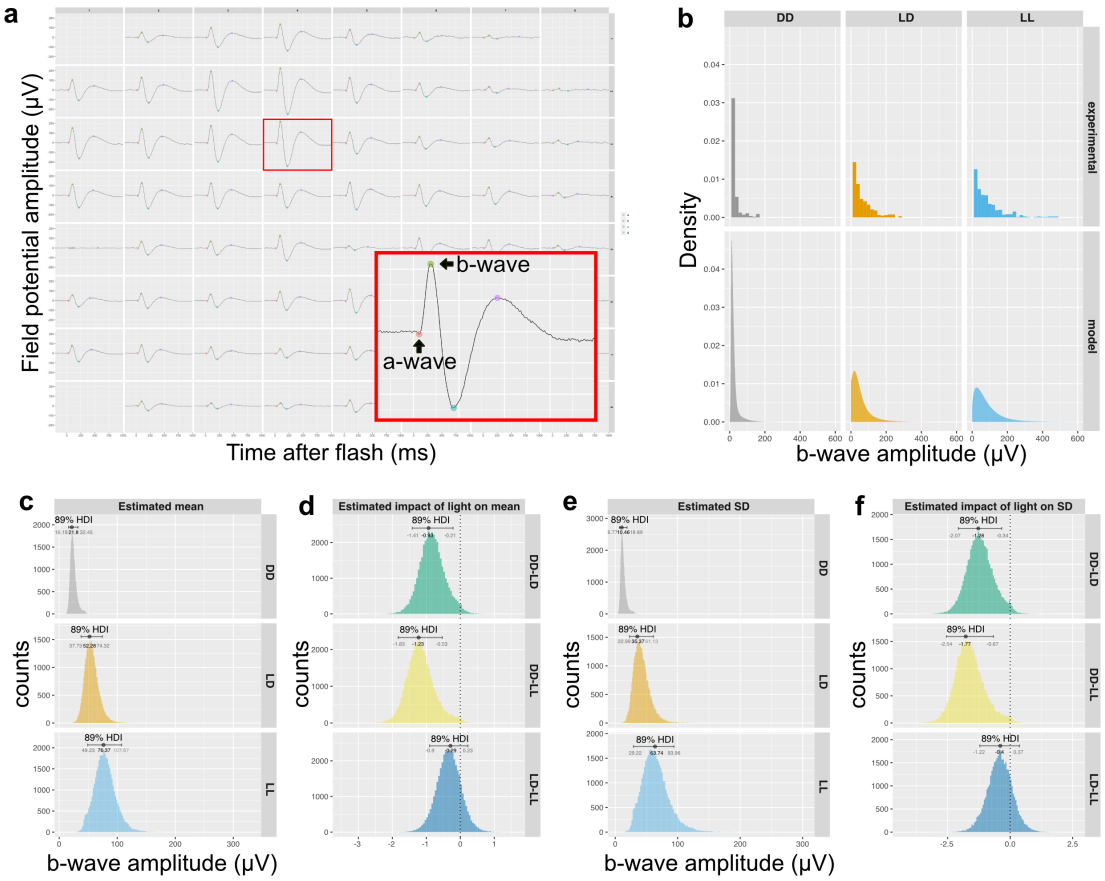
a
Field potential amplitude (μV)
Time after flash (ms)
b-wave
a-wave
b
DD
LD
LL
experimental
model
Density
b-wave amplitude (μV)
c
Estimated mean
d
Estimated impact of light on mean
e
Estimated SD
f
Estimated impact of light on SD
89% HDI
counts
b-wave amplitude (μV)

Fig. 5

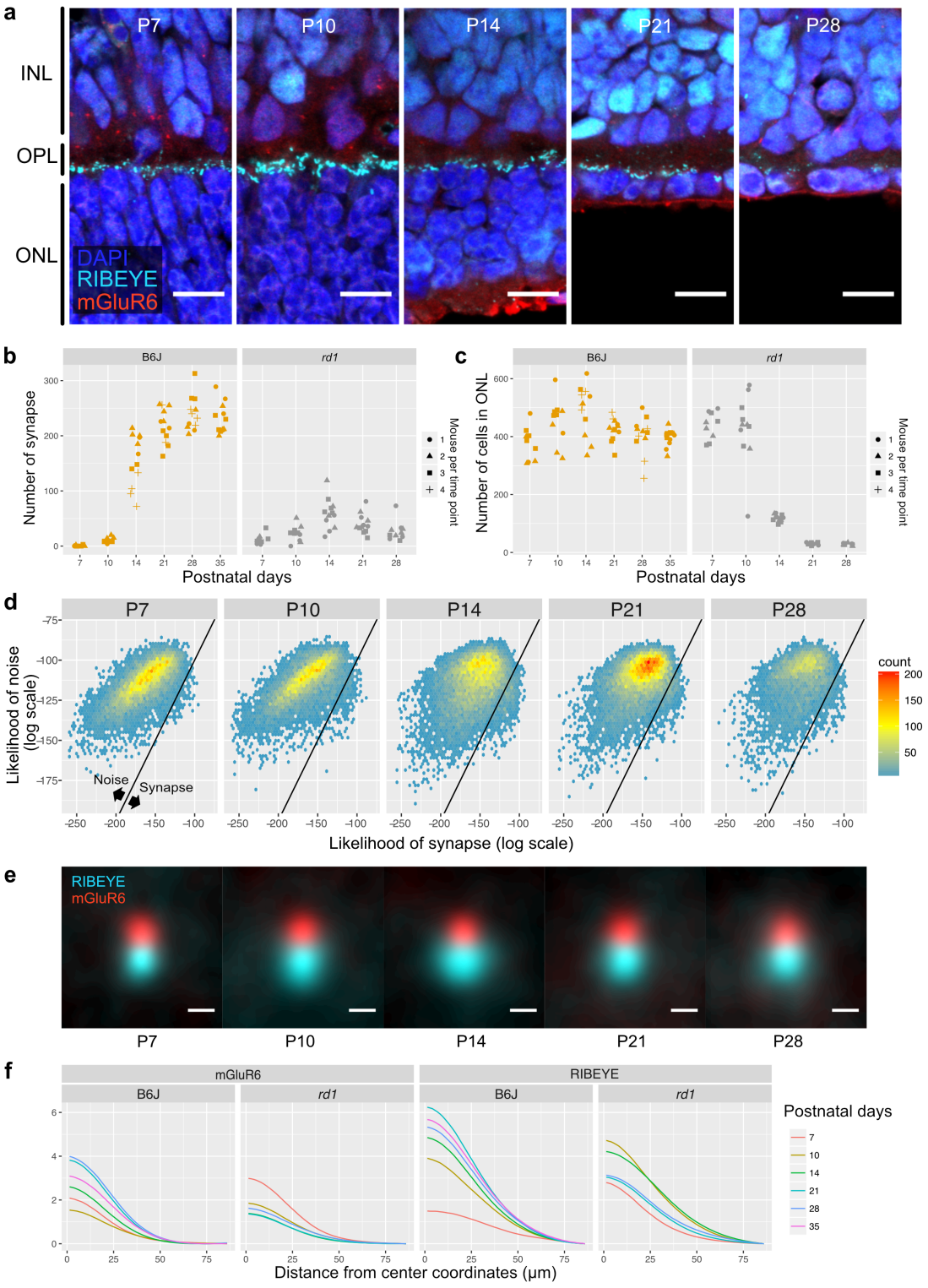
a
P7
P10
P14
P21
P28
INL
OPL
ONL
DAPI
RIBEYE
mGluR6
b
B6J
rd1
Number of synapse
Postnatal days
Mouse per time point
c
Number of cells in ONL
d
Likelihood of noise (log scale)
Likelihood of synapse (log scale)
Noise
Synapse
count
e
RIBEYE
mGluR6
f
mGluR6
RIBEYE
Distance from center coordinates (μm)
Postnatal days

Fig. 6

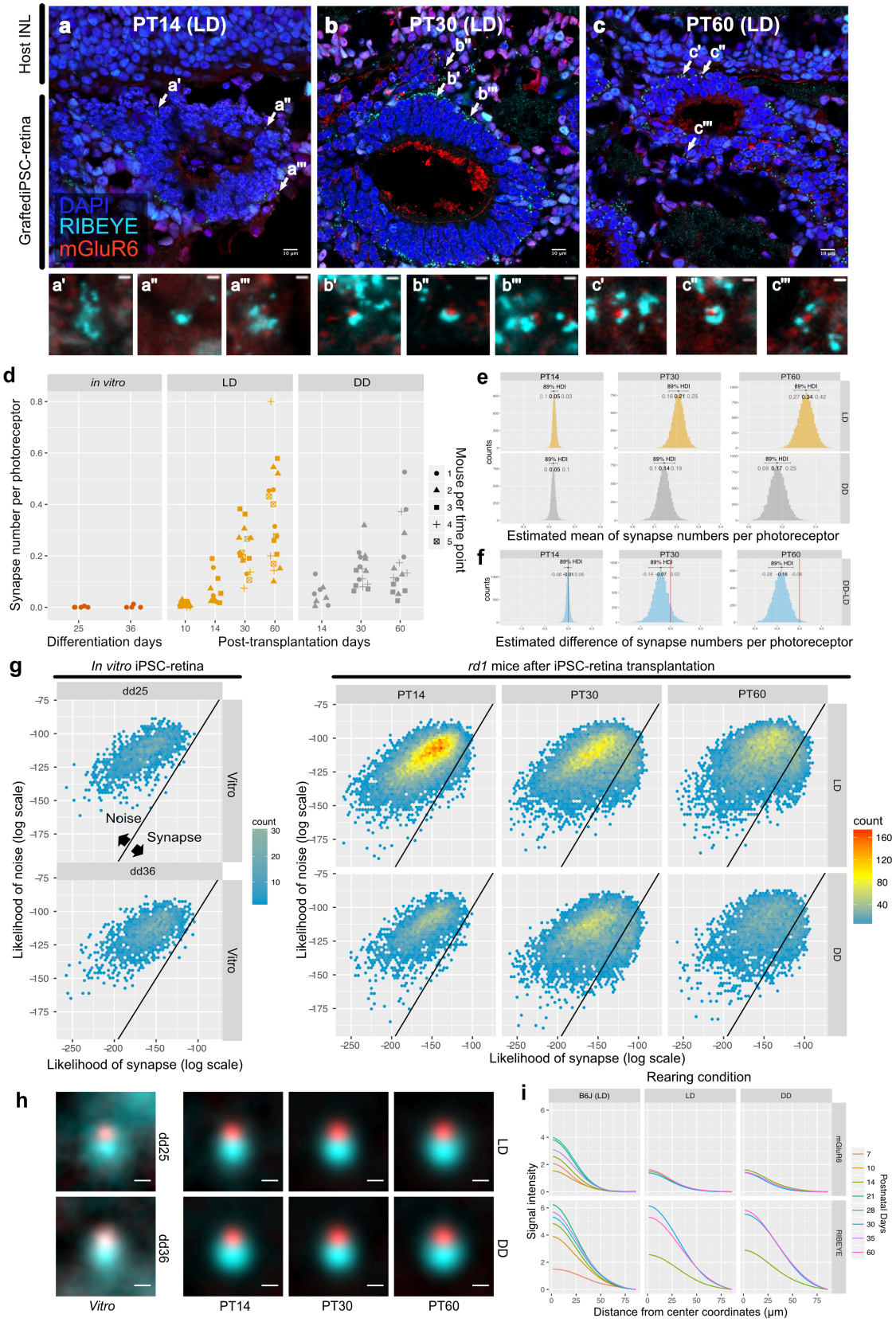
Host INL
GraftediPSC-retina
a PT14 (LD)
b PT30 (LD)
c PT60 (LD)
DAPI
RIBEYE
mGluR6
d
in vitro
LD
DD
Synapse number per photoreceptor
Differentiation days
Post-transplantation days
Mouse per time point
e
Estimated mean of synapse numbers per photoreceptor
f
Estimated difference of synapse numbers per photoreceptor
g
In vitro iPSC-retina
rd1 mice after iPSC-retina transplantation
dd25
dd36
Noise
Synapse
Likelihood of noise (log scale)
Likelihood of synapse (log scale)
count
h
dd25
dd36
Vitro
PT14
PT30
PT60
i
Rearing condition
B6J (LD)
Signal intensity
Distance from center coordinates (μm)
Postnatal Days

Fig. 7

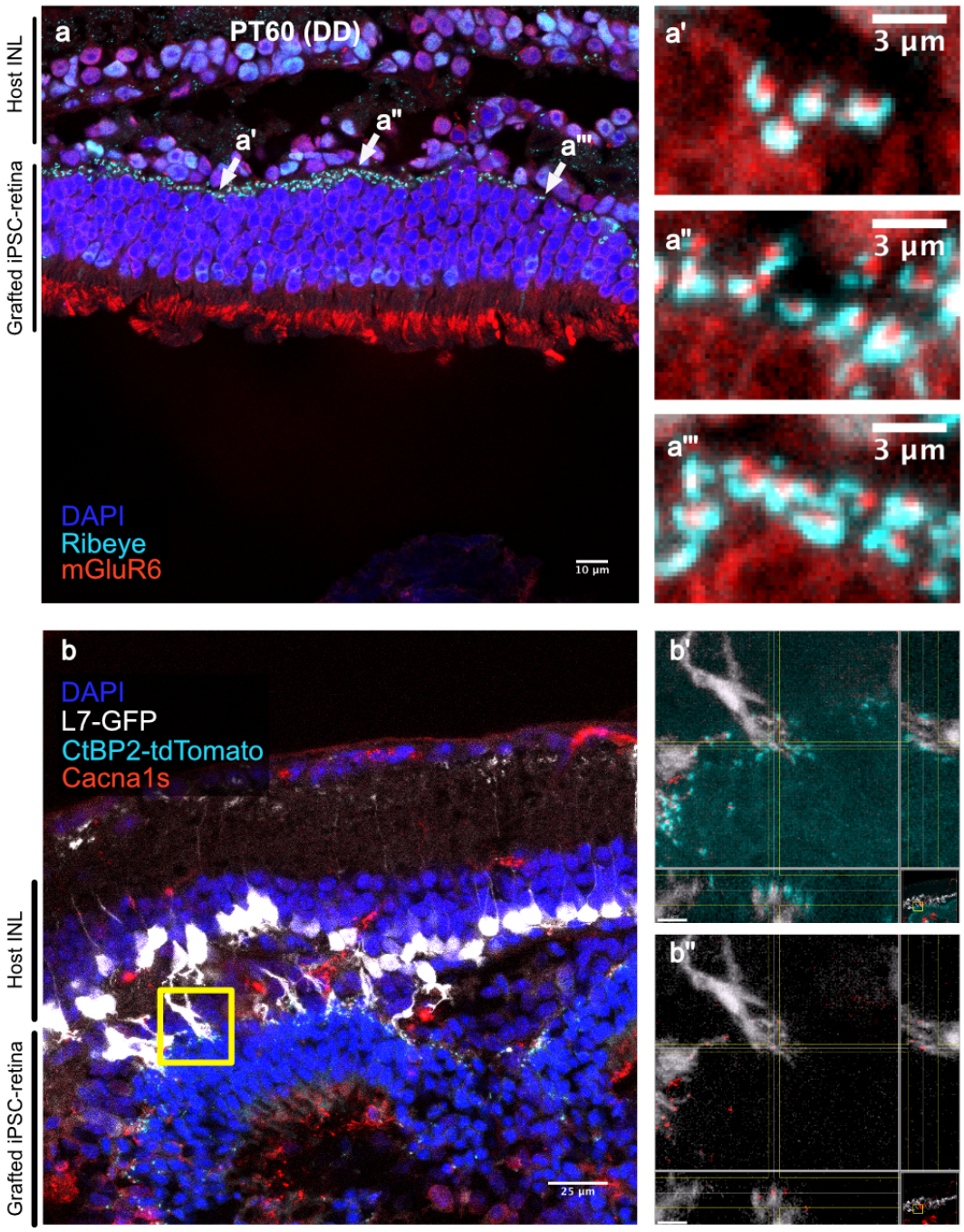
a
PT60 (DD)
a'
a"
a'''
Host INL
Grafted iPSC-retina
DAPI
Ribeye
mGluR6
10 µm
a'
3 µm
a"
3 µm
a'''
3 µm
b
DAPI
L7-GFP
CtBP2-tdTomato
Cacna1s
Host INL
Grafted iPSC-retina
25 µm
b'
b"

Fig. 8

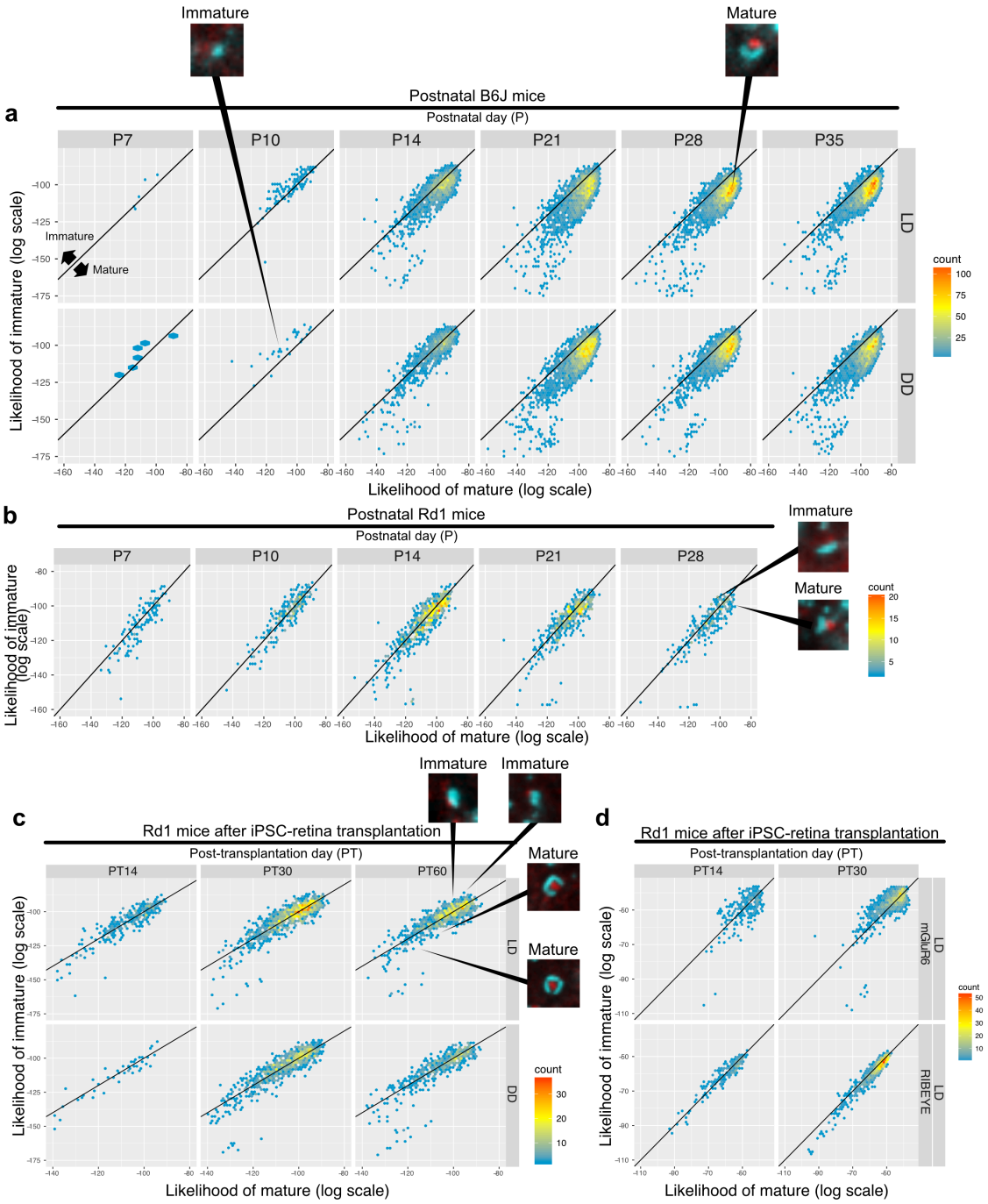
a
Immature
Mature
Postnatal B6J mice
Postnatal day (P)
P7
P10
P14
P21
P28
P35
LD
DD
count
Likelihood of immature (log scale)
Likelihood of mature (log scale)
b
Postnatal Rd1 mice
Postnatal day (P)
c
Rd1 mice after iPSC-retina transplantation
Post-transplantation day (PT)
PT14
PT30
PT60
d
mGluR6
RIBEYE

Fig. S1

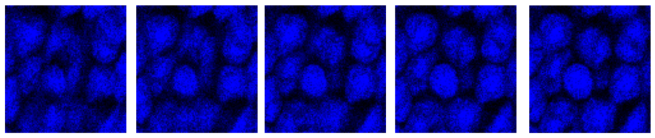

Raw images

Steps	Purpose of steps and detailed parameters
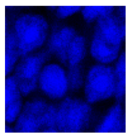 Z project of 5 images	Reduced the noise contained in each plane and, sum information of z-direction
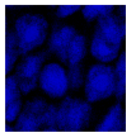 Subtract background	Reducing the backgound noise. Parameters are : roling=18
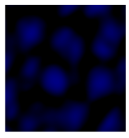 Bandpass filter	Normalizing the intensity variance inside each cell. Parameters are : filter_large= 32, filter_small=6, supress=None, tolerance=5
 Robust Automatic Threshold selection	To select the Region of interest. Among many threshold methods, RATS works the best with DAPI channel. Parameters are as follows: noise=3, lambda=1, min=205
 Dilate	Thresholding only selects strong ROI area, which lead to dropping the soma area, therefore dilatation is needed. "Binary > Option > Dilate" was used, and the iteration and count was both 1
 Adjustable watershed	Threshold and dilate cause merging of proximal cells. Adjustable watershed with tolerance 0.5 can split the merged cells. From this image, Region of Interest was generated using "Analyze Particle" function
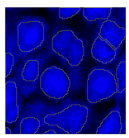 Analyze particle	Using previously generated ROI, graphical information of each ROI was extracted using "Measure" function

Fig. S2

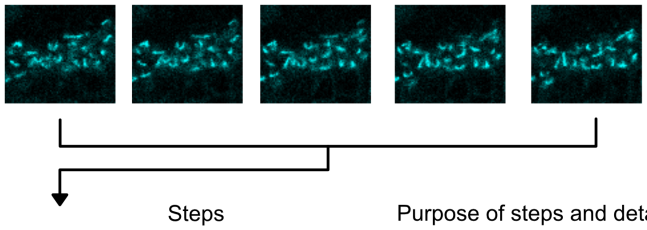

Raw images

Steps	Purpose of steps and detailed parameters
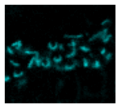 Z project of 5 images	Reduced the noise contained in each plane and, sum information of z-direction. "Average" method was used for projection.
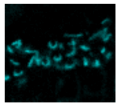 Subtract backgroud	In order to normalize the intensity by background intenstity, "Subtract Background" was done with parameter : rolling=10
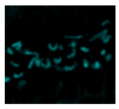 Bandpass filter	For making the edge smoother and make the signal inside marker more homogenous, bandpass filter was done with foloowing parameters : filter_large=20 filter_small=1 suppress=None tolerance=5
 Smoothing	For additinal smoothing for making thresholding easy, "Smooth" function was used.
 Segmented particle	Background intensity is heterogenous even in single image, therefore we segemented areas for each markers so that we can use the background intensity from the area around each markers. For segmentation , "Find Maxima" with noise=8, output=Segmented Particle was used.
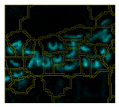 Find maxima	Background intensity was calcuated as follows: bg_intensity =(maximum intensity - minimum intensity) / 1.8
 Threshold	Using the estimated background intensity, we thresholded the image using "Find Maxima" function with following paraneters: noise=bg_intensity, output=Maxima Within Tolerance
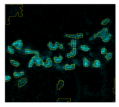 Analyze Particle	Using previously generated ROI, graphical information of each ROI was extracted using "Measure" function

Fig. S3

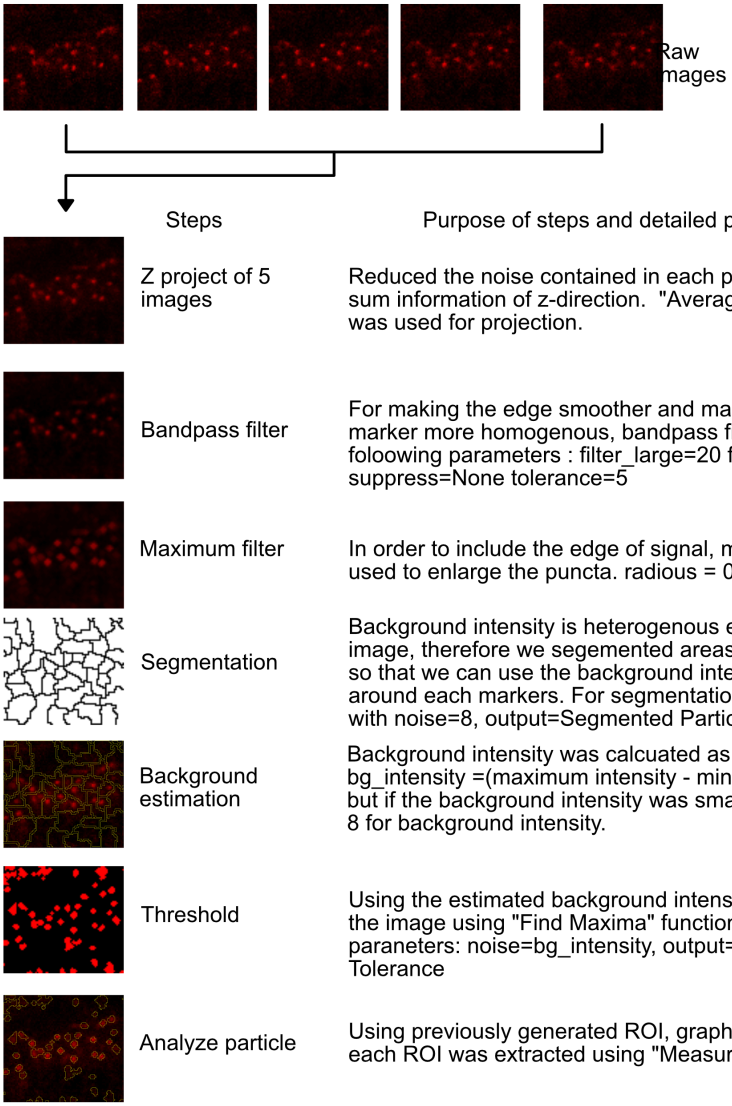
Raw
mages
Steps
Purpose of steps and detailed parameters
Z project of 5 images
Reduced the noise contained in each plane and, sum information of z-direction. "Average" method was used for projection.
Bandpass filter
For making the edge smoother and make the signal inside marker more homogenous, bandpass filter was done with foloowing parameters : filter_large=20 filter_small=1 suppress=None tolerance=5
Maximum filter
In order to include the edge of signal, maximum filter was used to enlarge the puncta. radious = 0.5
Segmentation
Background intensity is heterogenous even in single image, therefore we segemented areas for each markers so that we can use the background intensity from the area around each markers. For segmentation , "Find Maxima" with noise=8, output=Segmented Particle was used.
Background estimation
Background intensity was calcuated as follows: bg_intensity =(maximum intensity - minimum intensity)/2.6 but if the background intensity was smaller than 8, we used 8 for background intensity.
Threshold
Using the estimated background intensity, we thresholded the image using "Find Maxima" function with following paraneters: noise=bg_intensity, output=Maxima Within Tolerance
Analyze particle
Using previously generated ROI, graphical information of each ROI was extracted using "Measure" function

Fig. S4

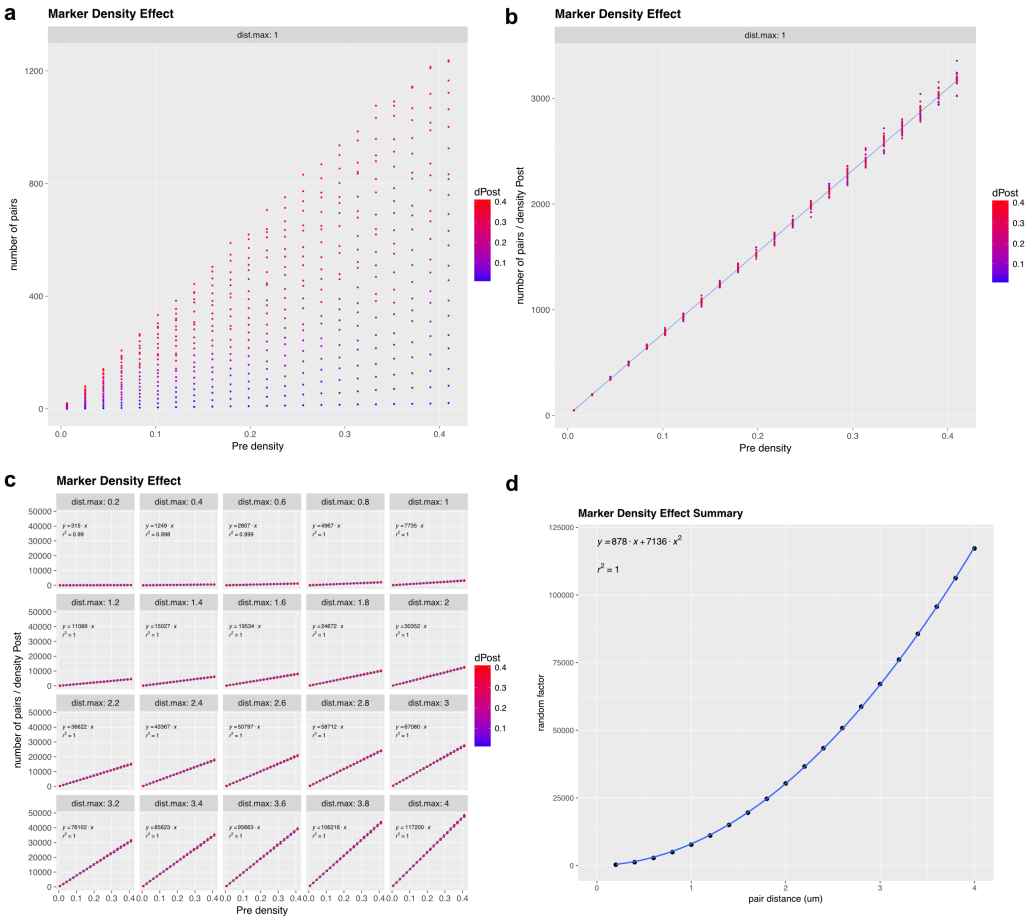
a
Marker Density Effect
dist.max: 1
number of pairs
Pre density
dPost
b
Marker Density Effect
dist.max: 1
number of pairs / density Post
Pre density
dPost
c
Marker Density Effect
dist.max: 0.2
dist.max: 0.4
dist.max: 0.6
dist.max: 0.8
dist.max: 1
dist.max: 1.2
dist.max: 1.4
dist.max: 1.6
dist.max: 1.8
dist.max: 2
dist.max: 2.2
dist.max: 2.4
dist.max: 2.6
dist.max: 2.8
dist.max: 3
dist.max: 3.2
dist.max: 3.4
dist.max: 3.6
dist.max: 3.8
dist.max: 4
number of pairs / density Post
Pre density
dPost
d
Marker Density Effect Summary
$y = 878 \cdot x + 7136 \cdot x^2$
$r^2 = 1$
random factor
pair distance (um)

Fig. S5


Geometry
Area (Pre)
Area (Post)
IntDen (Pre)
IntDen (Post)
IntDen_bg (Pre)
IntDen_bg (Post)
RawIntDen (Pre)
RawIntDen (Post)
RawIntDen_bg (Pre)
RawIntDen_bg (Post)
Morphology
Perimeter (Pre)
Perimeter (Post)
shape (Pre)
shape (Post)
AR (Pre)
AR (Post)
Round (Pre)
Round (Post)
Width (Pre)
Width (Post)
Height (Pre)
Height (Post)
Circularity (Pre)
Circularity (Post)
Solidity (Pre)
Solidity (Post)
Major (Pre)
Major (Post)
Minor (Pre)
Minor (Post)
FeretAngle (Pre)
FeretAngle (Post)
Feret (Pre)
Feret (Post)
Angle (Pre)
Angle (Post)
MinFeret (Pre)
MinFeret (Post)
Signal
Mean (Pre)
Mean_bg (Pre)
Mean_z (Pre)
StdDev (Pre)
StdDev_bg (Pre)
StdDev_z (Pre)
Mean (Post)
Mean_bg (Post)
Mean_z (Post)
StdDev (Post)
StdDev_bg (Post)
StdDev_z (Post)
Median (Pre)
Median_bg (Pre)
Median_z (Pre)
Min (Pre)
Min_bg (Pre)
Min_z (Pre)
Median (Post)
Median_bg (Post)
Median_z (Post)
Min (Post)
Min_bg (Post)
Min_z (Post)
Mode (Pre)
Mode_bg (Pre)
Mode_z (Pre)
Max (Pre)
Max_bg (Pre)
Max_z (Pre)
Mode (Post)
Mode_bg (Post)
Mode_z (Post)
Max (Post)
Max_bg (Post)
Max_z (Post)
Skew (Pre)
Skew (Post)
Kurt (Pre)
Kurt (Post)

Frontiers in Cellular Neuroscience

doi: 10.3389/fncel.2019.00016

平成31年1月16日　受理